

Effect of framework composition and NH_3 on the diffusion of Cu^+ in Cu-CHA catalysts predicted by machine-learning accelerated molecular dynamics

Reisel Millan,^{†,‡} Estefanía Bello-Jurado,[¶] Manuel Moliner,[¶] Mercedes Boronat,^{*,¶} and Rafael Gomez-Bombarelli^{*,†}

[†]*Department of Materials Science and Engineering, Massachusetts Institute of Technology, Cambridge, MA 02139*

[‡]*Universitat Politècnica de València*

[¶]*Instituto de Tecnología Química, Universitat Politècnica de València-Consejo Superior de Investigaciones Científicas, Avenida de los Naranjos s/n, 46022 Valencia, Spain*

E-mail: boronat@itq.upv.es; rafagb@mit.edu

Abstract

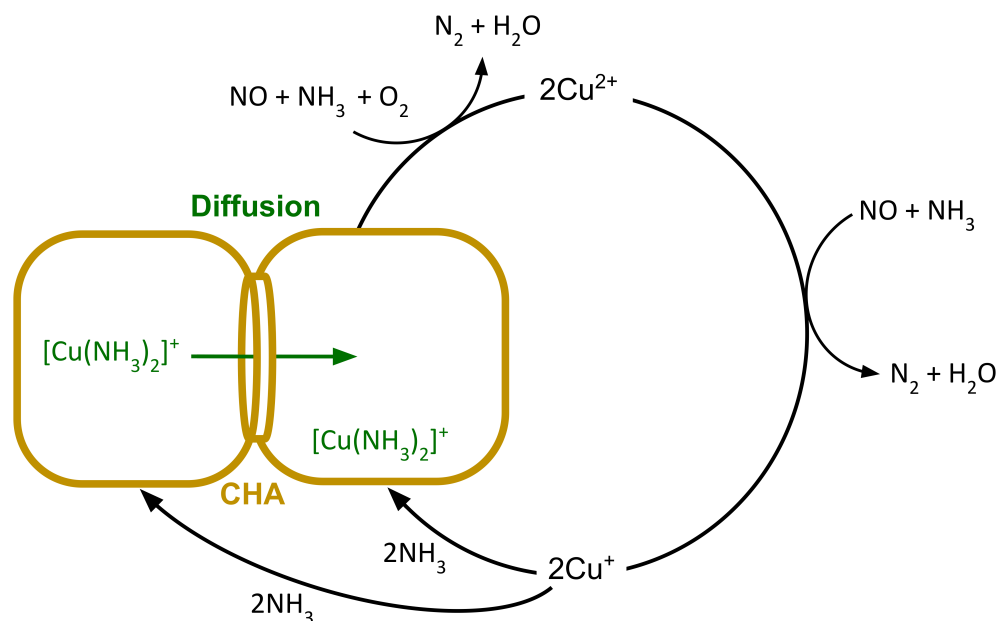
Cu-exchanged zeolites rely on mobile solvated Cu^+ cations for their catalytic activity, but the role of framework composition on transport is not fully understood. Ab initio molecular dynamics simulations can provide quantitative atomistic insight but are too computationally expensive to explore large length- and time-scales or diverse compositions. We report a machine-learning interatomic potential that accurately reproduces ab initio results and effectively generalizes to allow multi-nanosecond simulations of large supercells and diverse chemical compositions. Biased and unbiased simulations of $[\text{Cu}(\text{NH}_3)_2]^+$ mobility show that aluminum pairing in eight-membered

rings accelerates local hopping, and demonstrate that increased NH_3 concentration enhances long-range diffusion. The probability of finding two $[\text{Cu}(\text{NH}_3)_2]^+$ complexes in the same cage - key for SCR-NOx reaction - increases with Cu content and Al content, but does not correlate with the long-range mobility of Cu^+ . Supporting experimental evidence was obtained from reactivity tests of Cu-CHA catalysts with controlled chemical composition.

Copper-exchanged zeolites play a crucial role as redox catalysts for some environmentally relevant processes, like the partial methane oxidation to methanol or the selective catalytic reduction of nitrogen oxides with ammonia (NH_3 -SCR-NOx). In both cases, the small pore Cu-SSZ-13 zeolite with the CHA structure has been reported as an efficient catalyst.¹⁻¹¹

The NH_3 -SCR-NOx reaction is currently employed for the removal of nitrogen oxides (NOx) from exhaust gases in diesel vehicles and stationary plants, through a redox catalytic cycle in which Cu^+ is oxidized to Cu^{2+} by NO_2 or $\text{NO}+\text{O}_2$, and then reduced to Cu^+ by reaction of NH_3 and NO forming harmless $\text{N}_2 + \text{H}_2\text{O}$ (Scheme 1).¹²⁻¹⁵ This understanding of the reaction mechanism has enabled development of optimized catalysts by tuning framework topology, composition and copper speciation. In the as-prepared catalysts, Cu^+ and Cu^{2+} cations are directly coordinated to the zeolite framework forming heterogeneous active sites, while under reaction conditions NH_3 solvates the Cu^+ cations forming mobile $[\text{Cu}(\text{NH}_3)_2]^+$ complexes that act as dynamic active sites, resembling homogeneous catalysts but within the confinement of the zeolite pores. At low temperature ($T < 523$ K) the oxidation step involves transient dimeric $\text{Cu}^+(\text{NH}_3)_2-\text{O}_2-\text{Cu}^+(\text{NH}_3)_2$ species whose formation requires the simultaneous presence of two $[\text{Cu}(\text{NH}_3)_2]^+$ monomers in the same *cha* cage. The hops between adjacent *cha* cages are modulated by size exclusion effects and also by the attractive interaction between the positively charged $[\text{Cu}(\text{NH}_3)_2]^+$ complexes and the negatively charged framework Al sites.^{8,9,15-17} Thus, structural properties like Al content and distribution, Cu loading or Brønsted acid site density, as well as the interaction of the Cu active sites with the reactants, in particular NH_3 , might affect the mobility of Cu cations

and consequently the $\text{NH}_3\text{-SCR-NO}_x$ reaction rate. This has been evidenced by recent studies combining catalytic activity tests with *operando* XAS or EPR spectroscopy,^{18–22} and *ab initio* molecular dynamics (AIMD) simulations have been successfully applied to provide atomistic insight into the dynamic nature of the Cu^+ cations under reaction conditions.^{9,16,17}



Scheme 1: Illustration of the low temperature SCR-NO_x redox cycle.

The cost of AIMD simulations limits their applicability to a few selected systems at a time, at small length- and time- scales. The timescale limitation may be partially bypassed with enhanced sampling methods, such as umbrella sampling (US), which have been used to study the slow diffusion of copper complexes in CHA.^{9,17} However, the systematic exploration of parameters such as Si/Al ratio, Al distribution, Cu/Al ratio, NH_3 concentration or the presence of Brønsted acid sites and compensating NH_4^+ cations has not been yet possible.

Machine learning (ML) has demonstrated broad applicability in materials science^{23,24} and heterogeneous catalysis.^{25–28} Machine learning potentials (MLPs), when trained with a sufficiently large and diverse dataset, can match the accuracy of quantum chemistry methods at a fraction of the computational cost.^{29–35} This allows the study of larger and more realistic

systems and more complex scientific problems,^{24,36-38} in particular those requiring the use of molecular dynamics simulations.³⁹⁻⁴¹ A broad variety of MLPs based on neural networks - so called neural network potentials (NNPs) - have been developed in the last years: ANI,⁴²⁻⁴⁵ Deep Tensor Neural Networks,⁴⁶ SchNet,⁴⁷ DeepPotentialNet,⁴⁸ MEGNet,⁴⁹ DimeNet,⁵⁰ OrbNet,⁵¹ PaiNN,⁵² NequIP,⁵³ and successfully used to study solids systems,^{37,54-56} ion diffusion,⁵⁷ and chemical reactions.⁵⁸⁻⁶⁰

Here, we leveraged these innovations and trained an NNP capable of describing $[\text{Cu}(\text{NH}_3)_2]^+$ species in aluminosilicate CHA with varying composition and NH_3 concentration. The trained NNP proved accurate and transferable, and acquiring all the training data was less costly than one traditional AIMD simulation. Biased MD simulations reproduced free energy profiles from DFT, and provided insight into transport for over a dozen combinations of Al distribution and NH_4^+ presence. Unbiased MD simulations were scaled to thousands of atoms for nanoseconds, and achieved a more realistic representation of the importance of Al density and distribution, Cu loading, and adsorbed NH_3 on the mobility of Cu^+ cations in Cu-CHA catalysts.

These results show that the activation free energy for $[\text{Cu}(\text{NH}_3)_2]^+$ hops between adjacent cages is lower for windows containing Al pairs, but also that this is a local effect with only weak influence on long-range mobility. $[\text{Cu}(\text{NH}_3)_2]^+$ migration to remote cages requires the simultaneous displacement of charge-compensating NH_4^+ which show a lower mobility that is enhanced by excess NH_3 . Lastly, simulations with large supercells show that the probability of finding two $[\text{Cu}(\text{NH}_3)_2]^+$ complexes in the same cage, a pre-requisite for the SCR-NOx reaction, increases with Cu loading, and also with the Al content in the zeolite. We confirm these trends experimentally through catalytic tests of Cu-CHA samples with controlled Si/Al and Cu/Al ratios.

Results

Neural network potential

NNPs are highly accurate but they struggle to extrapolate outside their training data. In order to ensure robust and accurate production simulations, our NNP was trained on data gathered through multiple generations of active learning (AL) using a query by-committee approach.⁶¹⁻⁶⁹ A committee (ensemble) of NNPs was trained on the available labeled data at each iteration, and new data was collected based on the disagreement (variance) of the prediction of the committee members on newly generated geometries, as described in Computational Details Section and illustrated in Figure 1a. The last generation of the NNP was trained on a complete dataset containing 42k revPBE+D3 force calculations on structural models with a diverse set of atomic local environments, ranging from 290 to 323 atoms per supercell, summarized in Table S1 (see structural models in Figure S1). The chemical compositions in the dataset (Figure 1b) cover a range of Si/Al ratio from 47 to 13. All DFT calculations in the training data were electrically neutral with negative charges arising from Al substitution being compensated by $[\text{Cu}(\text{NH}_3)_2]^+$, NH_4^+ , or H^+ .⁷⁰⁻⁷²

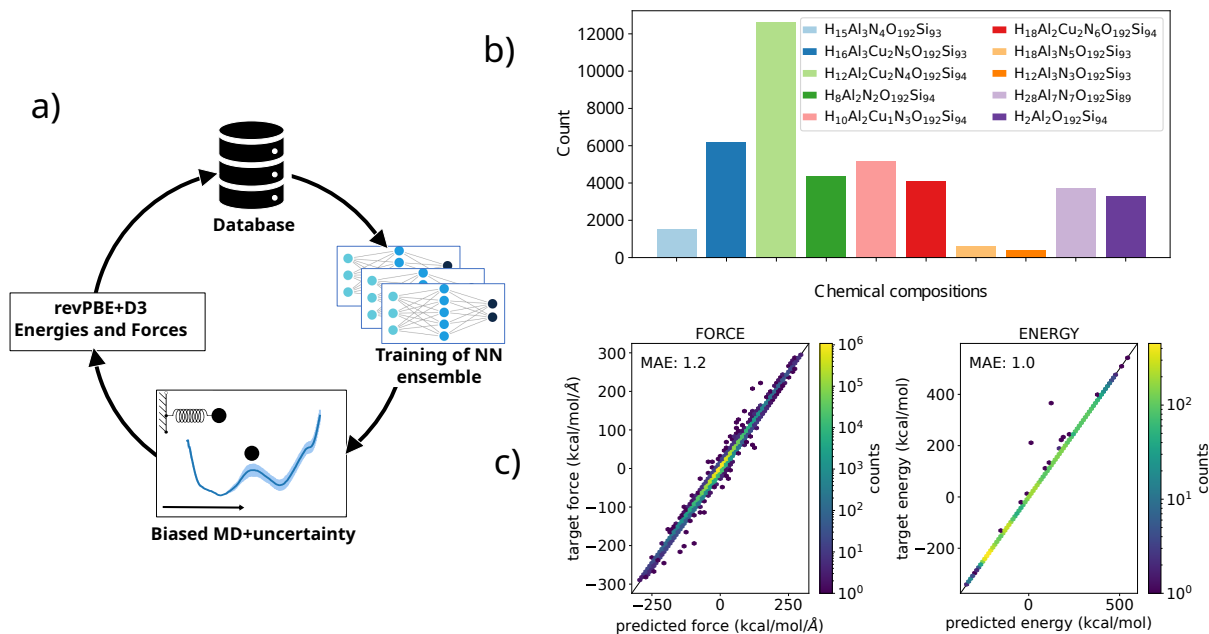


Figure 1: Neural Network Potential. (a) Illustration of the active learning cycle. (b) Distribution of the chemical composition of the dataset. (c) Correlation between the predicted and target energies (left) and forces (right) of the last generation potential.

The active learning strategy was capable of automatically adding new, diverse, and informative chemical environments to the training pool at each of the pre-selected compositions through a combination of MD and uncertainty quantification. It generated informative training data for a number of chemical processes that occur during the reaction, but were not present in the initial training data. These include adsorption and protonation of NH_3 on the Brønsted acid sites to form NH_4^+ cations, exchange between a gas phase NH_3 molecule and one of the two NH_3 ligands of the $[\text{Cu}(\text{NH}_3)_2]^+$ complex, and proton transfer from NH_4^+ to NH_3 . The diffusion of $[\text{Cu}(\text{NH}_3)_2]^+$ complexes through the 8R windows that connect adjacent *cha* cages has a higher activation barrier. Therefore representative training data was obtained through the same enhanced sampling approach as the production simulations (Figure S2).

This strategic combination of biased MD with uncertainty quantification allowed efficient sampling of the relevant regions on the PES with a small and diverse number of DFT evaluations. Figure S3 illustrates the structural diversity in the final dataset by means of

a 2D projection of the local chemical environments around each Al atom in our data using UMAP⁷³ on the feature vectors learned by the NNP.⁷⁴ Atoms with similar local environments have similar feature vectors and appear close on the UMAP plot. The overlap among the chemical compositions suggests a nearly continuous sampling of the Al local environment.

Figure 1d shows the correlation between predicted and target energies and forces for a held-out test set. The mean absolute error of the predicted energies and forces are 0.98 kcal/mol and 1.2 kcal/mol/Å respectively, indicating that the NNP is capable of predicting the energies and forces with chemical accuracy.

Effect of Al distribution on $[\text{Cu}(\text{NH}_3)_2]^+$ diffusion through 8R windows from biased simulations

The favorable speed of the NNP accelerates US MD simulations by orders of magnitude over DFT, and enabled systematic exploration of the role of Al distribution in well converged simulations. Ten different structural models with $\text{H}_{12}\text{Al}_2\text{Cu}_2\text{N}_4\text{O}_{192}\text{Si}_{94}$ composition were built (Fig 2a), each containing two framework Al atoms compensated with two $[\text{Cu}(\text{NH}_3)_2]^+$, and distributed either in the same 8R (SR1, SR2, SR3 and SR4), in different 8Rs (DR1, DR2, DR3 and DR4), in the same 4R (S4R) or in the same 6R (S6R).

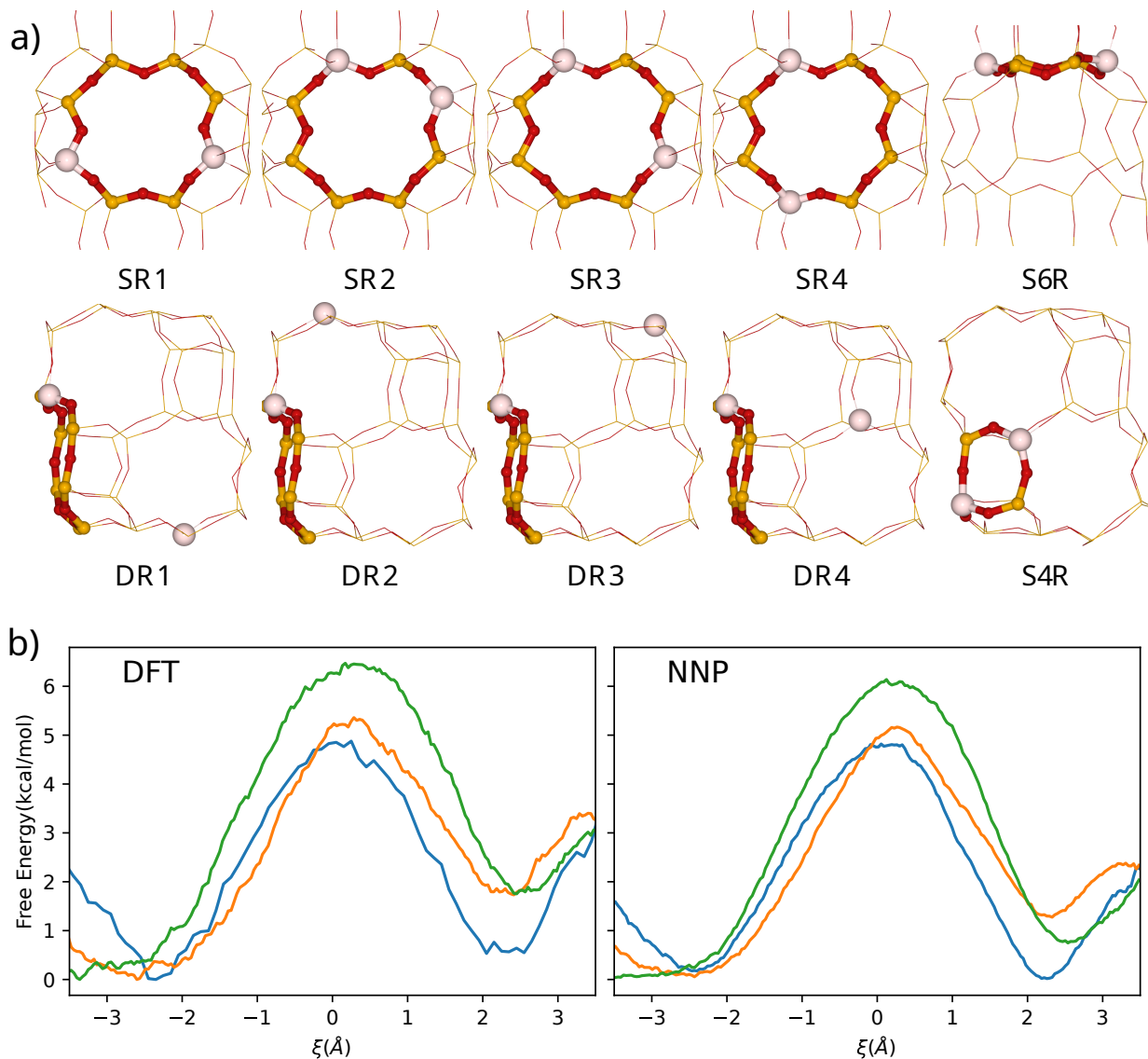


Figure 2: Structural models and accuracy of NNP biased simulations. (a) Representation of the different Al pair distributions used in the biased simulations. The atoms in the ring containing the Al pair are highlighted. Si, O and Al atoms are depicted in orange, red and light brown, respectively. (b) Comparison of free energy profiles for $[\text{Cu}(\text{NH}_3)_2]^+$ diffusion through the 8R window of SR1 (orange), SR4 (blue) and DR2 (green) systems obtained from DFT (left) and NNP (right) based biased simulations at 423 K.

Because the error of the predicted forces is not a sufficient metric for true performance in production simulations,⁷⁵ the NNPs were further validated by comparing NNP and DFT free energy profiles for $[\text{Cu}(\text{NH}_3)_2]^+$ diffusion through the 8R window of DR2, SR1 and SR4. Due to the high computational cost of producing reference DFT biased simulations, a

smaller hexagonal 126-atom unit cell was used. The free energy profiles for SR1, SR4 and DR2 (Figure 2b) and the calculated activation free energies (ΔG_{act}), 5.2 and 5.3 kcal/mol for SR1, 4.8 and 4.8 kcal/mol for SR4, and 6.1 and 6.4 kcal/mol for DR2, are in excellent agreement at both computational levels.

The smoother NNP traces are a consequence of more abundant sampling (4.8 ns total, compared to 0.8 for DFT) given the advantageous computational cost of NNP (20 ps of AIMD required over a week on CPU cores (Intel(R) Xeon(R) CPU E5-2650 v3 @ 2.30GHz), compared to 20 min on a Tesla V100-32 GB GPU for NNP).

Then, the free energy profiles for $[\text{Cu}(\text{NH}_3)_2]^+$ diffusion between neighboring cages in the ten systems depicted in Figure 2a were obtained from NNP biased simulations at 423 K using the larger $\text{H}_{12}\text{Al}_2\text{Cu}_2\text{N}_4\text{O}_{192}\text{Si}_{94}$ models. The profiles are plotted in Figure 3 and the corresponding values of activation (ΔG_{act}) and reaction (ΔG) free energies are summarized in Table S2. The shaded area in each profile shows the standard error calculated from three independent simulations using three different NNPs trained on the same dataset. The average value of the standard error, 0.1 kcal/mol in all cases, indicates a low uncertainty in the prediction of the free energy and well-converged statistics.

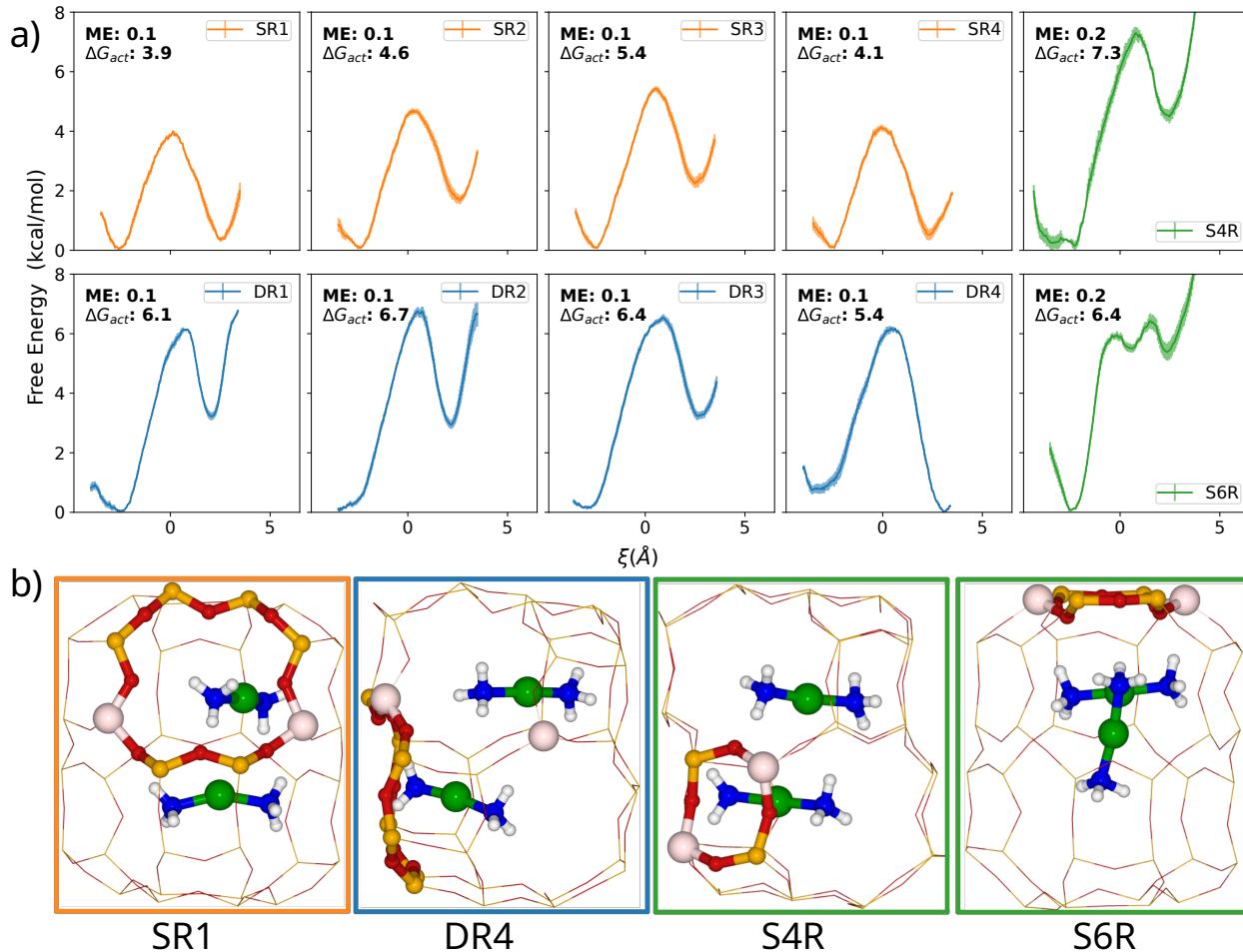


Figure 3: NNP biased simulations of $[\text{Cu}(\text{NH}_3)_2]^+$ diffusion. (a) Free energy profiles for the diffusion of one $[\text{Cu}(\text{NH}_3)_2]^+$ complex from a cage A to a neighboring cage B occupied by another $[\text{Cu}(\text{NH}_3)_2]^+$ complex and (b) snapshots of the final state at $\xi = 2.5$ corresponding to the diffusion of $[\text{Cu}(\text{NH}_3)_2]^+$ through the 8R windows of SR1, DR4, S4R and S6R systems at 423 K.

For the systems with two Al atoms in the same 8R (orange profiles in Figure 3), ΔG_{act} values range from 3.9 to 5.4 kcal/mol and the reaction is slightly endergonic with ΔG values between 0.4 and 2.3 kcal/mol. In all other cases, ΔG_{act} are higher than 6 kcal/mol and ΔG are larger than 3 kcal/mol, with the only exception of the DR4 system for which the process is slightly exergonic. The Al distribution in the DR4 model is the same as in SR1, but the diffusion occurs through different 8R windows (see snapshots in Figure 3). In both cases, the stability of the final state with the two $[\text{Cu}(\text{NH}_3)_2]^+$ in the same cage is similar to that of the initial state with the two complexes in different cages, which suggests that this

particular Al distribution might favor the formation of the $[\text{Cu}(\text{NH}_3)_2]^+ - \text{OO} - [\text{Cu}(\text{NH}_3)_2]^+$ dimers involved in the low-temperature NH_3 -SCR-NOx reaction. In contrast, distributions with two Al in the same 4R or 6R hinder the formation of such dimeric intermediates, because only one of the two $[\text{Cu}(\text{NH}_3)_2]^+$ can stay near the Al atoms (see snapshots in Figure 3) while the second $[\text{Cu}(\text{NH}_3)_2]^+$ is forced to remain in too close contact with the first, resulting in its diffusion through a different 8R to another empty cage. These results demonstrate that Al distribution affects the movement of $[\text{Cu}(\text{NH}_3)_2]^+$ species between cages and the stability of pairs of $[\text{Cu}(\text{NH}_3)_2]^+$ complexes in the same cage, and points to a positive effect of Al pairs in 8R on the rate of the low-temperature NH_3 -SCR-NOx reaction.

Effect of NH_4^+ on the diffusion of $[\text{Cu}(\text{NH}_3)_2]^+$ through 8R windows from biased simulations

The mobility of $[\text{Cu}(\text{NH}_3)_2]^+$ complexes within the zeolite microporous structure is affected by the presence of other molecules involved in the reaction, among which NH_3 is the most abundant and the one with the largest impact on diffusion and reactivity.^{16,17,20,21,76,77} Under reaction conditions NH_3 is readily protonated on the Brønsted acid sites forming NH_4^+ cations that remain coordinated to the framework AlO_4^- units and might partly block the diffusion of $[\text{Cu}(\text{NH}_3)_2]^+$ complexes through the 8R windows. To analyze this possibility we first performed NNP biased simulations at 423 K using the previously described $\text{H}_{10}\text{Al}_2\text{Cu}_1\text{N}_3\text{O}_{192}\text{Si}_{94}$ models with two framework Al atoms compensated now with one $[\text{Cu}(\text{NH}_3)_2]^+$ complex and one NH_4^+ cation. The free energy profiles obtained for the three Al distributions considered (SR1, SR2 and SR3), plotted in Figure 4 are clearly different from those depicted in Figure 3, and the calculated activation free energies for $[\text{Cu}(\text{NH}_3)_2]^+$ diffusion are also reflective of how the strong coordination of NH_4^+ modifies transport.

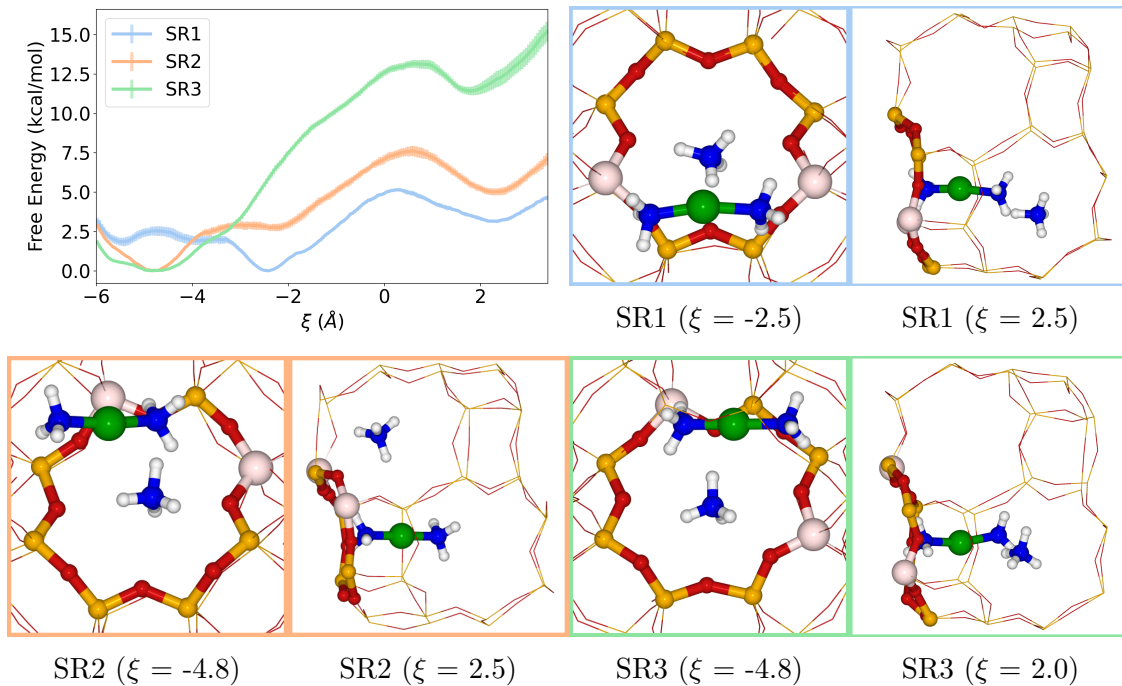


Figure 4: Effect of NH_4^+ on the diffusion of $[\text{Cu}(\text{NH}_3)_2]^+$ complex. Free energy profiles for $[\text{Cu}(\text{NH}_3)_2]^+$ diffusion between neighboring cages in the presence of NH_4^+ in three different systems obtained from NNP-based biased simulations at 423 K, and snapshots of the systems SR1, SR2 and SR3 at the initial and final minimum states. Si, O, Al, H, Cu and N atoms are depicted in orange, red, light brown, white, green and blue, respectively.

Whereas in the previous simulations without NH_4^+ the most stable minimum for the initial state occurs at $\xi \sim -2.5 \text{ \AA}$, with $[\text{Cu}(\text{NH}_3)_2]^+$ relatively close to the 8R, that is the case only for SR1 in the presence of NH_4^+ . In SR2 and SR3 models the most stable minimum lies at $\xi \sim -4.8 \text{ \AA}$, with the $[\text{Cu}(\text{NH}_3)_2]^+$ complex closer to the center of the cavity and farther away from the 8R to be crossed and therefore from the negatively charged AlO_4^- units. The calculated ΔG_{act} , 5.2, 7.6 and 13.1 kcal/mol for SR1, SR2 and SR3, respectively, and ΔG values, 3.2, 5.0 and 11.4 kcal/mol for SR1, SR2 and SR3, respectively, are higher than those obtained for the corresponding systems in the absence of NH_4^+ . The snapshots of the final state at $\xi \sim 2.5 \text{ \AA}$ for SR1 and SR2 in Figure 4 show that the NH_4^+ cation has been displaced from its initial position in the plane of the 8R to a position relatively close to one of the AlO_4^- units. In SR3, however, the NH_4^+ cation has been displaced to the opposite side of the cage, far from the two AlO_4^- sites present in the model, which would explain the

instability of the system. The deviation across replicate profiles is wider in some regions, which we attribute to the fact that our simulations occasionally, but not exhaustively, sample the spontaneous reversible deprotonation of NH_4^+ cations to form NH_3 and a Brønsted acid site, which is typically not accessible to traditional simulations.

Altogether, the results from the biased simulations suggest a potential blocking effect of NH_4^+ cations. However, their own mobility, as either NH_4^+ or NH_3 following proton transfer to deprotonated AlO_4^- , and possible migration from the 8R towards other nearby AlO_4^- units that are not present in this model might modify this conclusion. The NNPs developed here open the possibility of running long-time unbiased MD simulations on larger systems with more realistic chemical compositions, allowing to capture the dynamics of $[\text{Cu}(\text{NH}_3)_2]^+$ and NH_4^+ globally and to observe long-range diffusion of both cationic species.

Long-range diffusion of NH_4^+ and $[\text{Cu}(\text{NH}_3)_2]^+$ species from unbiased MD simulations

A large $\text{T}_{768}\text{O}_{1536}$ supercell of dimension $\sim 37 \text{ \AA}$ was used to construct eight models representing three Al contents, low (L), medium (M) and high (H), two copper loadings (4 and 20 atoms per simulation box), and varying NH_3 , NH_4^+ and H^+ concentrations and Al pairings as described in Methods Section, Fig 5 and Table S3. Unbiased MD simulations at 500 K were conducted for at least 5 ns on each 2000-atom system.

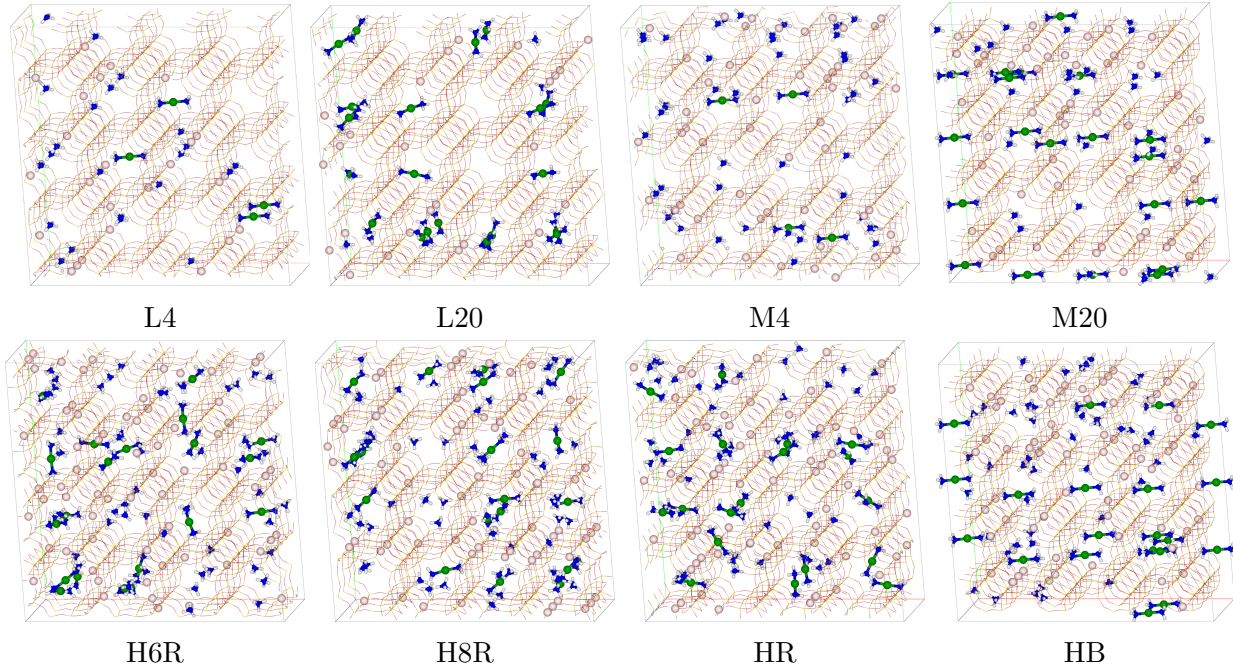


Figure 5: Structural models used in NNP unbiased MD simulations. Snapshots of the input structures corresponding to the eight different zeolite framework compositions considered. The first letter of the label indicates the Al content, L (low) Si/Al=28.5, M (medium) Si/Al=14.3 and H (high) Si/Al=10.3. The number in the top models indicates the Cu loading, 4 or 20 atoms per unit cell. The second letter in the bottom models that contain 20 Cu atoms per unit cell indicates the Al distribution, forming pairs in 6R or 8R, random (R) and biased (B). Si, O, Al, H, Cu and N atoms are depicted as orange, red, light brown, white, green and blue.

Figures 6 a and b track, respectively, the time evolution of the mean square displacements (MSDs) of the N atoms in the NH_4^+ cations and of the Cu atoms in the $[\text{Cu}(\text{NH}_3)_2]^+$ complexes. While both species have a net charge of +1, $[\text{Cu}(\text{NH}_3)_2]^+$ is much more mobile while NH_4^+ cations are more closely attached to the AlO_4^- units (Figs S4 and S5). This is due to the positive charge in $[\text{Cu}(\text{NH}_3)_2]^+$ complexes being highly shielded by the two NH_3 ligands.

The similarity among the MSD profiles of N atoms suggests that the mobility of NH_4^+ cations is rather independent of zeolite framework composition and Cu content (Figure 6a), while the MSD traces for Cu (Figure 6b) suggest slightly lower mobility of $[\text{Cu}(\text{NH}_3)_2]^+$ in the systems with high Al content (Si/Al \sim 10, Figure 6b). The trends are similar in

the number of distinct cages visited by the $[\text{Cu}(\text{NH}_3)_2]^+$ complex over time (Figure 6c), but they are more stratified and more clearly show an increase in mobility with decreasing copper content (orange and red dashed lines higher than solid in Fig 6c). In 5 ns, each $[\text{Cu}(\text{NH}_3)_2]^+$ complex visits on average fewer than three different cages in the models with high Al content, which increases to 3-4 for intermediate Al, and reaches a maximum of over 5 different cages visited for the L4 model, which has the lowest Al content and thus few Al pairs in 8R. This is in apparent contradiction to the biased simulations results for small models, that showed lower hopping free energy barrier for Al pairing in 8R. A potential explanation is that the hopping landscape is statically and dynamically heterogeneous, with the local chemical environment of each initial and final cages, and transient cage occupation by other mobile molecules influencing the mobility of copper complexes. Fig S4 shows the diversity in length and tortuosity in example trajectories of Cu atoms inside the zeolite microporous structure. While MSD profiles representing the average movement of the $[\text{Cu}(\text{NH}_3)_2]^+$ species are relatively similar across catalyst models ($\sim 40\text{-}60 \text{ \AA}^2$), the local mobility of each individual $[\text{Cu}(\text{NH}_3)_2]^+$ complex depends on its local chemical environment.

Since all framework AlO_4^- units are compensated with either $[\text{Cu}(\text{NH}_3)_2]^+$ or NH_4^+ , lower Cu content implies larger NH_4^+ concentration for a given Si/Al ratio. Comparison of L4 with L20, and M4 with M20 in Figure 6c suggests that NH_4^+ assists the long-range diffusion of $[\text{Cu}(\text{NH}_3)_2]^+$. A proposed explanation is that adsorbed NH_4^+ shields the attractive interaction between AlO_4^- anionic sites and the $[\text{Cu}(\text{NH}_3)_2]^+$ complexes. Each NH_4^+ forms two strong hydrogen bonds with the AlO_4^- site, hence the lower mobility of NH_4^+ while $[\text{Cu}(\text{NH}_3)_2]^+$ interacts with the zeolite through the H atoms of the coordinating NH_3 molecules. This "crowding" of the anionic sites by the harder NH_4^+ can be observed statistically in the simulations. The average distances between the Cu atoms and the closest framework Al atoms plotted in Figure 6d are $\sim 4.5 \text{ \AA}$ in the L and M models (orange and red lines), and increase to $\sim 5.0 \text{ \AA}$ in the systems with higher Al content and thus a larger amount of charge-balancing NH_4^+ (green lines). The HB model has a heterogeneous Al

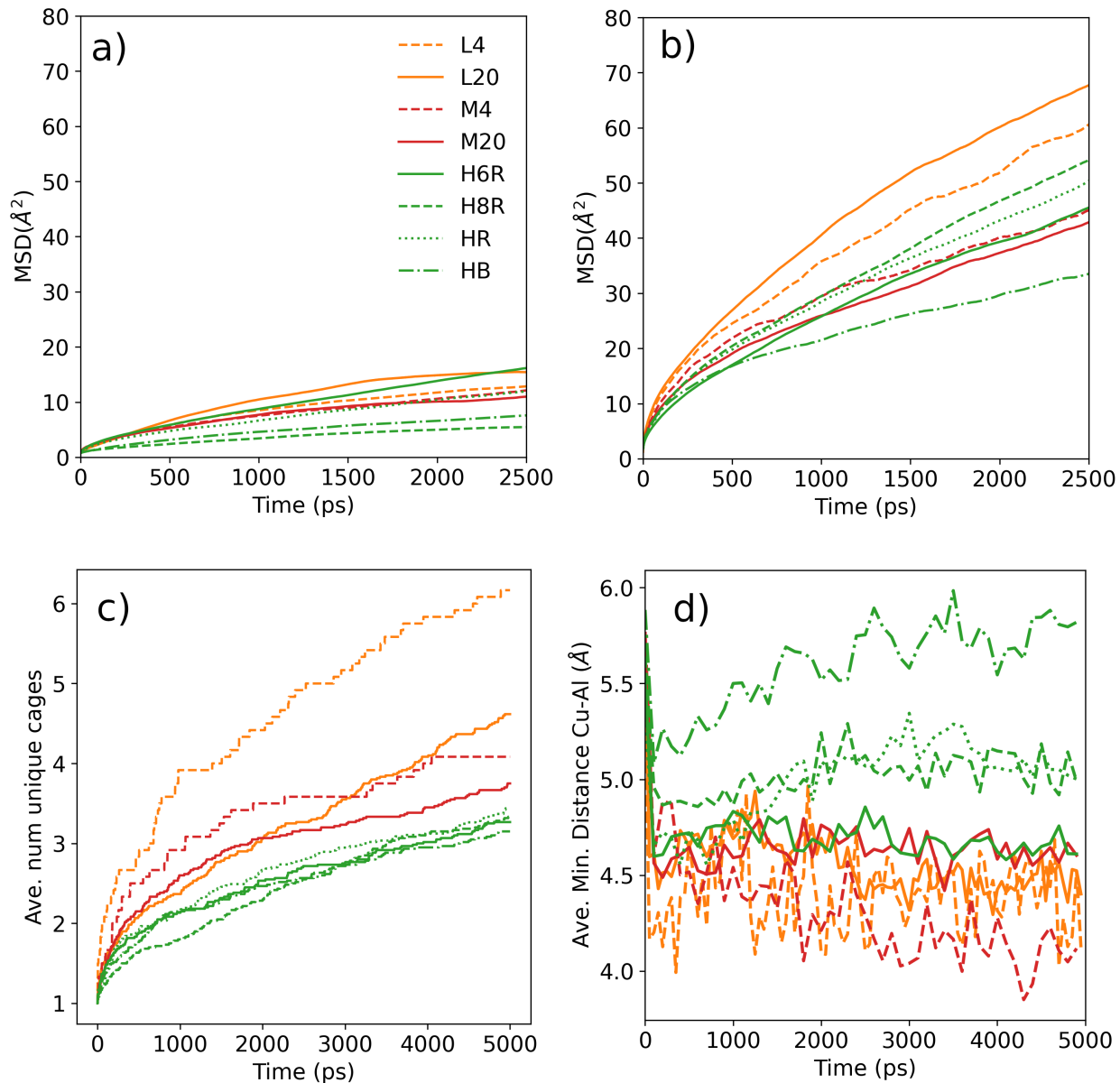


Figure 6: Mobility of NH_4^+ and $[\text{Cu}(\text{NH}_3)_2]^+$. (a) Mean square displacement (MSD) of N atoms in NH_4^+ (b) MSD of Cu atoms in the $[\text{Cu}(\text{NH}_3)_2]^+$ complexes obtained from NPP-based unbiased MD simulations at 500 K. (c) Number of distinct cages visited by the Cu atoms. The apparent contradiction with the MSD plots is explained by the fact that the diffusion of $[\text{Cu}(\text{NH}_3)_2]^+$ does not occur along a preferential direction. One Al pair in a 8R can accelerate the diffusion of $[\text{Cu}(\text{NH}_3)_2]^+$ between two neighboring cages in multiple forward and backward steps, so that only two distinct cages are visited by this complex. (d) average minimum Cu-Al distances. All plots were obtained from the same simulations. MSD was calculated using eq 1.

distribution and its anomalously high Cu-Al distance is due to $[\text{Cu}(\text{NH}_3)_2]^+$ complexes in Al-poor regions.

Previous studies have suggested that $[\text{Cu}(\text{NH}_3)_2]^+$ migration is fast only between the three cages sharing a common framework Al, while long-range diffusion to non-adjacent cages is limited to $\sim 9 \text{ \AA}$ due to decaying electrostatic to the $[\text{Cu}(\text{NH}_3)_2]^+$ and the anionic AlO_4^- site.^{9,17,19} This argument is rigorously true when the final cages contain no additional Al sites, as our model systems from the first section. In real systems, however, the long-range diffusion is easily explained through a sequence of local steps combining the crossing of 8R windows into adjacent Al-containing cages, followed by the exchange of NH_4^+ as compensating cation (Scheme S1 in the Supporting Information). The low mobility of NH_4^+ revealed by the present simulations suggests that a limiting factor for such long-range diffusion of $[\text{Cu}(\text{NH}_3)_2]^+$ complexes is the slower rate of counter-migration of the charge-compensating NH_4^+ . While $[\text{Cu}(\text{NH}_3)_2]^+$ could act as a migrating compensating cation, this results in no net migration of copper.

To explore this hypothesis, two additional MD simulations of 5 ns were run using two modified M20 models, one of them containing 30 protons as compensating cations, labeled M20-H+, and another one with 60 additional NH_3 molecules added to the system, labeled M20-NH3. Protons on the Brønsted acid sites are fairly static and localized within the four O atoms directly attached to Al, so long-range charge-compensation diffusion of H^+ should be hindered. In contrast, additional NH_3 should facilitate the movement of the positive charges via proton transfer from NH_4^+ to NH_3 via a Grotthuss-like chain of proton transfers, thus allowing faster charge compensation between separated AlO_4^- units without the need of physically displacing the strongly attached NH_4^+ cations.

The plots in Figure 7 confirm this hypothesis. The MSD of Cu atoms in Figure 7a does not change when NH_4^+ cations are substituted by protons (black lines) with a similar electrostatic shielding effect as NH_4^+ . However, copper mobility increases significantly in the presence of excess NH_3 molecules (brown lines), suggesting that free NH_3 facilitates the

charge re-equilibrium following $[\text{Cu}(\text{NH}_3)_2]^+$ crossing 8R. In keeping, the average distances between the Cu atoms and the closest framework Al atoms increases from $\sim 4.5 \text{ \AA}$ to $\sim 6.0 \text{ \AA}$ with the added NH_3 (Figure 7b). Lastly, the number of distinct cages visited by $[\text{Cu}(\text{NH}_3)_2]^+$ (Figure 7c) indicates again a slightly lower long-range mobility of $[\text{Cu}(\text{NH}_3)_2]^+$ in the model containing Brønsted acid sites and enhanced diffusion in the presence of an excess of NH_3 .

Our results provide theoretical backing to recent experimental observations of the enhancing effect of gas phase NH_3 during the solid-state ion-exchange of copper using mixtures of copper oxides and zeolites, which allows the fast preparation of Cu-exchanged zeolites at low temperatures (473-523 K).^{76,77} After $\sim 4000 \text{ ps}$ the three models reached similar steady states with ~ 3.5 distinct cages being visited by each complex, corresponding to the final state of the ion-exchange process with a random distribution of $[\text{Cu}(\text{NH}_3)_2]^+$ complexes occupying the whole unit cell.

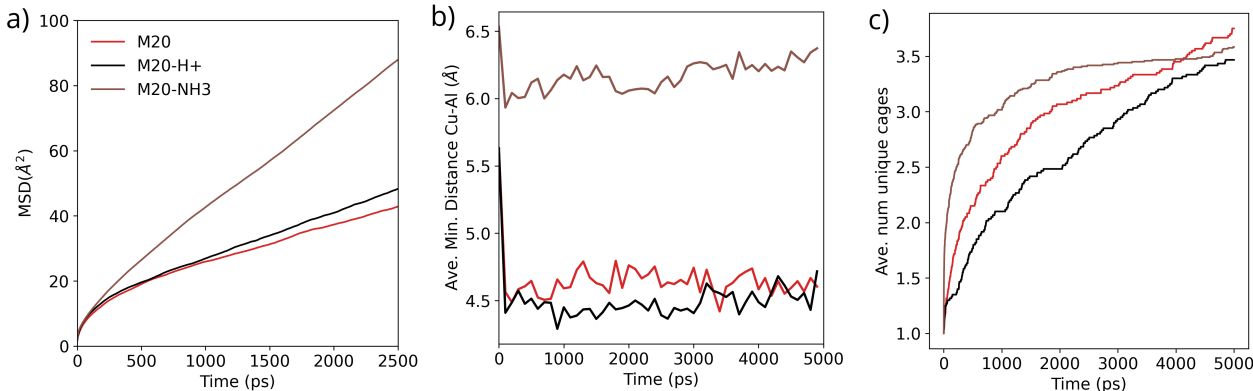


Figure 7: Influence of framework charge shielding on the mobility of $[\text{Cu}(\text{NH}_3)_2]^+$. (a) Mean square displacement (MSD) of Cu atoms in the $[\text{Cu}(\text{NH}_3)_2]^+$ complexes, (b) average minimum Cu-Al distances and (c) number of distinct cages visited obtained from NPP-based unbiased MD simulations at 500 K in models with different charge-compensating cations and additional NH_3 molecules. MSDs were calculated using eq 1.

Bimolecular complexes and mechanistic implications for the NH_3 -SCR- NO_x reaction

According to the proposed mechanism,⁹ the reaction rate depends directly on the probability of finding simultaneously two $[\text{Cu}(\text{NH}_3)_2]^+$ complexes in the same cage, which we analyzed separately from the mobility calculations.

Figure 8a tracks the time evolution of the average number of $[\text{Cu}(\text{NH}_3)_2]^+$ pairs present simultaneously within the same *cha* cage. As expected, the probability of having two $[\text{Cu}(\text{NH}_3)_2]^+$ complexes in the same cage directly correlates with the total amount of Cu in the system (compare L4 with L20 or M4 with M20 models). More interestingly, for a given Cu loading, the average number of $[\text{Cu}(\text{NH}_3)_2]^+$ pairs in the same cage increases with increasing the Al content in the system (compare L4 with M4 or L20 with M20). This trend runs opposite to our observation about the number of distinct cages visited, which was highest for the model with lowest Al and lowest Cu content. That is, the chemical environments that result in a higher rate of long-range diffusion of copper complexes do not result in formation of more pairs, or by extension in higher reactivity, .

As regards the role of Al distribution, the four models with a Si/Al ratio ~ 10 and different Al pairings (H6R, H8R, HR, HB) (see Methods Section, Fig 5 and Table S3) behave similarly and the plots in Figure 8a only suggest a lower probability of finding two $[\text{Cu}(\text{NH}_3)_2]^+$ in the same cage in the H6R model with Al pairs in the 6R windows, and perhaps a slightly higher probability of bringing two $[\text{Cu}(\text{NH}_3)_2]^+$ complexes together in the H8R model with Al pairs in the 8R windows. The increased NH_3 loading in M20-NH3 also results in increased number of pairs (Figure S6).

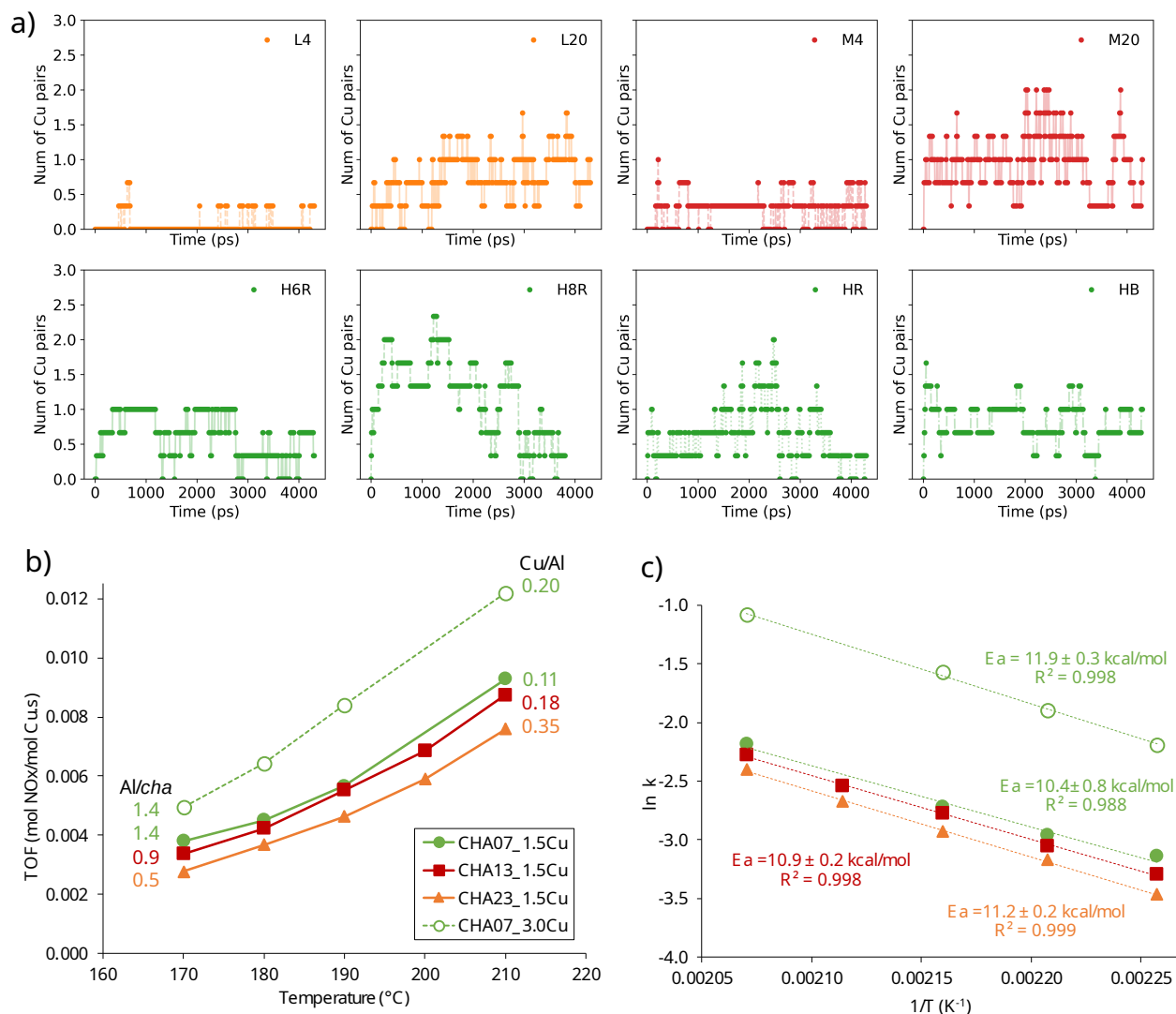


Figure 8: Probability of formation of the active sites and catalytic results for the $\text{NH}_3\text{-SCR-NO}_x$ reaction. (a) Time evolution of the average number of $[\text{Cu}(\text{NH}_3)_2]^+$ pairs in the same cage for the eight systems in Figure 5. The geometric center of every cage in the unit cell are determined and two Cu atoms are considered to be in the same cage when both have the same cage center as the nearest cage center. (b) Turnover frequency (TOF) values on a per Cu-ion basis for the $\sim 1.5\%$ wt Cu-containing zeolites with different Si/Al molar ratios (b) and CHA07 (Si/Al ~ 7) zeolite with two different Cu-contents (~ 1.5 and $\sim 3\%$ wt Cu) (c).

Experimental validation for the low-T NH₃-SCR-NO_x reaction catalyzed by Cu-CHA zeolites with controlled composition

To experimentally validate the computational predictions, three CHA samples with different Si/Al molar ratios ranging from 7.3 to 23.3, which translates to a broad range of 1.4 to 0.5 Al sites per *cha* (see Table S4 in the Supporting Information) were synthesized as described in Methods. Then, the same Cu loading ($\sim 1.5\%$ wt Cu) was introduced within the three CHA materials, which resulted in a similar amount of initial Cu atoms per *cha* cage, ~ 0.17 , but different Cu/Al ratios (from 0.11 to 0.35, see Table S5). In addition, the CHA sample with Si/Al ratio ~ 7.3 was also loaded with 3.0% wt Cu resulting in an additional sample with increased amount of initial Cu atoms per *cha* cage (0.3).

The catalytic tests to evaluate the low-temperature SCR-NO_x activity of the different Cu-CHA materials were performed at very high space velocities (1800000 ml/h.great) to assure low NO conversions ($< 20\%$). Turnover frequency values (TOF) were obtained for each Cu-CHA sample at five different temperatures (see Figure 8b). The TOF values obtained for the three catalysts with different Si/Al molar ratio and the same Cu content ($\sim 1.5\%$ wt Cu) exhibit a continuous activity enhancement as the Al/*cha* cage ratio increases from 0.5 to 1.4 (see Figure 8b), in agreement with the theoretical conclusion that the probability of finding simultaneously two $[\text{Cu}(\text{NH}_3)_2]^+$ complexes in the same *cha* cage increases with increasing the Al content in the zeolite system. Comparison of the TOF values obtained for samples with the same Si/Al ratio and different Cu content (full and dotted green lines in Figure 8b) or even with similar Cu/Al ratio and different Cu content (red and dotted green line in Figure 8b) confirm that the catalytic activity clearly improves with increasing the Cu/*cha* ratio, in good agreement with the theoretical conclusion that the probability of forming $[\text{Cu}(\text{NH}_3)_2]^+$ pairs in the same *cha* cage directly correlates with the total amount of Cu in the system.

The experimental apparent activation energies (Figure 8c) are similar for all samples irrespective of the Si/Al ratio, Cu content or catalytic activity, ranging from 10.4 ± 0.8 to

11.9 ± 0.3 kcal/mol. The catalytic activity measured by the TOF and normalized by Cu content, however, increases in parallel with the calculated likelihood of two-copper encounters in the same cage (Fig 8a). This supports the argument that the formation of $[\text{Cu}(\text{NH}_3)_2]^+$ pairs in the same *cha* cage is responsible for the generation of the binuclear active sites that catalyze the reaction, although copper diffusion may not necessarily be the rate-determining step of the global process.

Conclusions

Biased and unbiased MD simulations using a newly trained NNP have achieved high accuracy, chemical diversity, length- and time scale, allowing the systematic investigation of the influence of catalyst composition and adsorbed NH_3 on the mobility of $[\text{Cu}(\text{NH}_3)_2]^+$ cations in Cu-CHA catalysts.

Biased simulations on small systems showed that single $[\text{Cu}(\text{NH}_3)_2]^+$ cation hops between adjacent *cha* cages are very sensitive to the Al distribution and, in general, Al pairs in 8R windows lower the free energy barrier for diffusion and stabilize the product configuration with two $[\text{Cu}(\text{NH}_3)_2]^+$ cations in the same cage. This might be taken to suggest that the rate of the SCR-NO_x reaction could be accelerated by selectively positioning the Al atoms as Al pairs. However, even though those results are well beyond the limits of traditional AIMD, the simulation cells employed are overly simple and lack realistic Al and NH_4^+ concentration.

Unbiased MD simulations using time scales of multiple nanoseconds and supercells with over 2300 framework atoms at a variety of Si/Al ratios, Cu^+ , NH_4^+ and NH_3 loadings show that $[\text{Cu}(\text{NH}_3)_2]^+$ cations can visit on average 3-4 cages and diffuse as far as 30 Å in a few nanoseconds. They also show that the long-range migration to remote cages requires the simultaneous displacement of a charge-compensating NH_4^+ cation. An excess of NH_3 facilitates the movement of the positive charges via proton transfer from NH_4^+ to NH_3 , thus enhancing the long-range diffusion of $[\text{Cu}(\text{NH}_3)_2]^+$ complexes.

Regarding catalytic activity, we observed that the probability of finding two $[\text{Cu}(\text{NH}_3)_2]^+$ complexes in the same cage, which is necessary for the SCR-NO_x reaction at low temperature, correlates directly with the Cu content and on the Al content but not so much on the Al distribution. These trends were confirmed experimentally through testing the SCR-NO_x reaction at low temperatures using Cu-CHA zeolites with different Si/Al and Cu/Al molar ratios, where we found increasing catalytic performance with increasing Al and Cu loading.

These results demonstrate the power of combining high-throughput DFT calculations, machine learning and molecular dynamics simulations for simulating transport in nanoporous catalysts. The collection of the training data and the training of the NNP had a lower total computational cost than a single traditional AIMD simulation and resulted in scalable, fast and accurate simulations.

This overall strategy is broadly applicable to other unsolved questions in nanoporous catalysts, since it enables DFT-accuracy, nanosecond-long MD simulations for thousands of atoms, and possibly beyond, by combining ML and enhanced sampling techniques.⁷⁸

Methods

Catalyst Models

The Cu-CHA catalytic system was modeled using three different supercells of increasing size (see Figure S1). The smallest system is a 1x1x1 hexagonal supercell of CHA framework containing 2Al, 34 Si and 72 O atoms, with lattice parameters, $a = b = 13.81 \text{ \AA}$, $c = 15.00 \text{ \AA}$, $\alpha = 89.86^\circ$, $\beta = 89.94^\circ$, $\gamma = 120.41^\circ$. Three models with different lattice distribution of the two Al atoms were created, and the two negative charges introduced by the presence of Al in the framework were compensated with two $[\text{Cu}(\text{NH}_3)_2]^+$ complexes (Figure 2a). These models were used to perform DFT-based umbrella sampling (US) molecular dynamics (MD) simulations and in the first generation of the NNP.

A 2x2x2 triclinic supercell containing 96 T and 192 O atoms, with lattice parameters

$a = 18.68 \text{ \AA}$, $b = 18.67 \text{ \AA}$, $c = 18.67 \text{ \AA}$, $\alpha = 94.68^\circ$, $\beta = 94.63^\circ$, $\gamma = 94.72^\circ$ was used for the subsequent training of the NN potentials including additional Al distributions, Al contents, and compensating species ($[\text{Cu}(\text{NH}_3)_2]^+$, NH_4^+ and H^+) as well as additional NH_3 molecules as summarized in Table S1. For the systems with 3 and 7 Al atoms, ten random Al distributions were generated. For the systems with two Al atoms ten different Al distributions were generated, one with 2 Al in the same 4R, one with two Al in the same 6R, four of them containing 2 Al in the same 8R, and four of them with the 2 Al in different rings. Single-point DFT calculations and NNP US-MD simulations were performed using this model.

Finally, a 4x4x4 triclinic supercell containing 768 T and 1536 O atoms, with lattice parameters $a = 37.35 \text{ \AA}$, $b = 37.38 \text{ \AA}$, $c = 37.34 \text{ \AA}$, $\alpha = 94.64^\circ$, $\beta = 94.59^\circ$, $\gamma = 94.47^\circ$ was employed to run NNP unbiased MD simulations on more realistic systems and reaction conditions. Three lattice compositions corresponding to $\text{Si}/\text{Al} \sim 30$ (26 Al, 742 Si and 1536 O atoms), $\text{Si}/\text{Al} \sim 15$ (50 Al, 718 Si and 1536 O atoms) and $\text{Si}/\text{Al} \sim 10$ (50 Al, 718 Si and 1536 O atoms) were considered, and for each of them three random Al distributions were generated. For the model with the highest Al content ($\text{Si}/\text{Al} \sim 10$), three additional Al distributions were generated in which all Al atoms were either forming pairs in the 6R units, forming pairs in the 8R windows, or heterogeneously distributed along the system so that Al-rich and Al-poor regions are found in the same unit cell. The negative charges in each model were compensated with $[\text{Cu}(\text{NH}_3)_2]^+$, NH_4^+ and H^+ as summarized in Table S3 in the Supporting Information. In the models with low and medium Al content, two Cu loadings were considered, 4 and 20 atoms per unit cell, corresponding to Cu spatial densities of 0.08 and 0.4 Cu/1000 \AA^2 respectively and 0.5% and 2.6% Cu/Si ratios (systems labeled L4, L20, M4 and M20, Figure 5). In the models with high Al content, the Cu loading was always 20 atoms per unit cell, and the labels in Figure 5 indicate the four different Al distributions considered, with Al pairs in the same 6R (H6R), with Al pairs in the same 4R (H4R), random distribution (HR) and a biased, spatially-heterogeneous distribution containing regions with high and low Al content (HB).

All DFT calculations (single points evaluations as well as the molecular dynamics simulations) were carried out at the revPBE+D3^{79,80} level of theory with the software CP2K.⁸¹ The Gaussian and Plane Waves (GPW) method⁸² was used with the TZVP basis set for all atoms except Cu, which was described with the DZVP-MOLOPT-SR-GTH basis set. A cutoff energy of 400 Ry was used for the auxiliary plane waves and the core electrons were represented with GTH pseudopotentials.⁸³

All NNP-MD simulations were performed using NNPs trained with the PaiNN⁵² architecture. Regular NNP-MD simulations were run in the NVT ensemble at 500 K, and consisted of a production run of at least 3 ns after 100 ps of equilibration. The temperature was controlled by a Nosé–Hoover chain thermostat^{84,85} with three beads and a time constant of 200 fs. The time step to integrate the equations of motion was set to 0.5 fs.

The mean squared displacements (MSD) obtained for $[\text{Cu}(\text{NH}_3)_2]^+$ and NH_4^+ were calculated via the following equation:

$$MSD(t) = \frac{1}{t_s - t + 1} \sum_{t_0=0}^{t_s=t} \frac{1}{N} \sum_{i=1}^N [r_i(t_0 + t) - r_i(t_0)]^2 \quad (1)$$

where N corresponds to the number of $[\text{Cu}(\text{NH}_3)_2]^+$ or NH_4^+ cations, t_s is the number of time steps in the simulation, the t_0 are the different time origins.

Gibbs free energy profiles for the diffusion of $[\text{Cu}(\text{NH}_3)_2]^+$ species through the 8R windows of Cu-SSZ-13 zeolite were obtained from umbrella sampling (US) simulations⁸⁶ at 423 K. The success of the US technique relies on the choice of a collective variable (CV) that represents unambiguously the process considered. It has been shown in the literature that the collective variable (ξ) that best describes the diffusion of $[\text{Cu}(\text{NH}_3)_2]^+$ from one cavity A ($\xi < 0$) to another one B ($\xi > 0$) is the projection of the position vector of the Cu atom on the vector normal to the average plane of the 8R (see Figure S2). This collective variable takes the value $\xi = 0$ when the Cu atom is located in the plane of the 8R. In the biased simulations, the collective variable ξ was split into 40 (for DFT-based simulations) or 80 (for

NN-based simulations) equidistant windows in the range $\xi = -4$ to $\xi = 4$. In each window, an independent biased MD simulation of 20 ps was run restricting the collective variable to one specific value but ensuring complete sampling of the configuration space in all other degrees of freedom. A harmonic bias potential centered at the corresponding value of the collective variable was applied to restrict the sampling to each window individually and to ensure sufficient overlap between the sampling of adjacent windows. The force constant of the harmonic potential was set to 12 kcal/mol/Å². All DFT-based biased simulations were performed with PLUMED⁸⁷ interfaced to the CP2K engine.

Neural network potential training

All NN potentials trained were based on the PaiNN architecture⁵² which uses equivariant message-passing for the ground truth prediction. For the training we used three convolutions, a cutoff radius of 5Å, 32 Gaussian functions for distance expansion and 128-size vector for the atomic features. Neural network parameters were optimized using Adam algorithm with a batch size of 32, initial learning rate of 1×10^{-4} , learning decay of 0.5 and learning patience of 25.

The reference energies of Si, Al, Cu, N, O, and H were evaluated using the revPBE+D3 energies of the lowest energy structure of each composition. These energies were used to fit a linear regression model with atomic contribution to the reference energy of each element as predictor variables. The reference energy was subtracted from the revPBE+D3 energy of every geometry in the training, test and validation sets. The forces were used without modifications. The training coefficients for the energies and the forces were set to 0.01 and 1.0, respectively.

The acquisition of training data was performed using active learning (AL) with a query-by-committee approach⁶¹⁻⁶⁸ as illustrated in Figure 1a. In this approach a committee (ensemble) of NNPs is trained on the available labelled data and new data is collected based on the maximum disagreement (variance) of the prediction the committee members.

The first generation of the potential was trained on a randomly collected subset of the DFT data generated from a previous study¹⁷ and from three biased simulations performed with DFT at 423 K, used as reference ground truth. In total, there were ~ 9000 geometries in the initial dataset. This pretrained potential was then retrained in 4 active learning loops using the 2x2x2 triclinic supercell described in previous section (see Figure S1. For each loop, biased MD trajectories were generated with the learned interatomic potential of the previous loop. The following temperatures were used in the active learning loops 298 K, 423 K, 500 K and 550 K. The bias was applied using a harmonic potential on the collective variable used in US. Each MD was run for 100 ps and geometries were collected every 100 fs. The selection of the new geometries from the MD trajectories was carried out using as criterion the force uncertainty from an ensemble of three NN potentials. The variances of the forces from the ensemble of potentials were ranked in descending order and the first geometries were selected to increase the dataset in $\sim 10\%$. The nonphysical geometries and those with low uncertainty, < 2 kcal/mol were discarded. Up to this point, the dataset contained structures where the Al substitutions were compensated with Cu^+ as diaminecopper(I) so that the trained potential did not properly describe local environments of Al compensated with NH_4^+ or H^+ . The acquisition of new geometries with new compositions including NH_4^+ and H^+ was performed using adversarial attack⁷¹ for 6 more generations with NNP trained on the last generation of AL. The initialization of adversarial attacks were performed by displacing each coordinate $\sigma \sim \text{N}(0, 0.01 \text{ \AA})$ of one optimized geometry for every chemical composition containing NH_4^+ and H^+ . The resulting attack σ was optimized for 100 iterations using the Adam optimizer with learning rate of 0.0001 and with the normalized temperature kT set to 20 kcal/mol.

Then, five more generations of active learning was performed, with biased MD simulations at temperatures ranging from 600 to 1000 K. All models were trained by randomly partitioning the available data into training (60%), validation (20%) and test sets (20%). This splitting was performed for each composition and then the training, test and valida-

tion sets of each composition were combined in the final training, test and validation sets. Thus, the final training, test and validation sets had a balanced distribution of all chemical compositions.

Zeolite synthesis

CHA zeolite with a Si/Al~7 (CHA07)

5.91 g of a 25 wt% aqueous solution of N,N,N-trimethyl-1-adamantylammoniumhydroxide (TMAda, Sachem) was added to 5.41 g of deionized H₂O. Next, 0.11 g of Al(OH)₃ (76.5 wt%, Thermo Fisher) and 0.85 g of a 5M sodium hydroxide solution (NaOH: 16.7 wt% NaOH in deionized water; NaOH pellets 98 wt%, Alfa Aesar) was added to the aqueous TMAdaOH solution and the mixture was stirred under ambient conditions for 15 minutes. Finally, 2.13 g of colloidal silica (Ludox HS40, 40 wt%, Sigma Aldrich) was added to the mixture and stirred for 2 h under ambient conditions. The final gel composition was: SiO₂ : 0.056 Al₂O₃ : 0.49 TMAdaOH : 0.25 NaOH : 46.5 H₂O. The resultant gel was charged into a stainless steel autoclave with a Teflon liner. The crystallization was then conducted at 160 °C for 6 days under dynamic conditions. The solid product was filtered, washed with abundant water, and dried at 100 °C. The solids were calcined at 580 °C for 5 h in air.

CHA zeolite with a Si/Al~13 (CHA13)

5.89 g of a 25 wt% aqueous solution of N,N,N-trimethyl-1-adamantylammoniumhydroxide (TMAda, Sachem) was added to 5.42 g of deionized H₂O. Next, 0.042 g of Al(OH)₃ (76.5 wt%, Thermo Fisher) and 0.86 g of a 5M sodium hydroxide solution (NaOH: 16.7 wt% NaOH in deionized water; NaOH pellets 98 wt%, Alfa Aesar) was added to the aqueous TMAdaOH solution and the mixture was stirred under ambient conditions for 15 minutes. Finally, 2.10 g of colloidal silica (Ludox HS40, 40 wt%, Sigma Aldrich) was added to the mixture and stirred for 2 h under ambient conditions. The final gel composition was: SiO₂ : 0.02 Al₂O₃ : 0.50 TMAdaOH : 0.26 NaOH : 47H₂O. The resultant gel was charged into a stainless steel

autoclave with a Teflon liner. The crystallization was then conducted at 160 °C for 6 days under dynamic conditions. The solid product was filtered, washed with abundant water, and dried at 100 °C. The solids were calcined at 580 °C for 5 h in air.

CHA zeolite with a Si/Al~23 (CHA23)

1.55 g of FAU zeolite (FAU, CBV760 with Si/Al=26, Zeolyst, lot number: 76004N002648) was added to 6.74 g of a 25 wt% aqueous solution of N,N,N-trimethyl-1-adamantylammoniumhydroxide (TMAda, Sachem). The mixture was maintained under stirring the required time to evaporate the excess of water until achieving the desired gel concentration. The final gel composition was: SiO₂ : 0.019 Al₂O₃ : 0.4 TMAdaOH : 5 H₂O. The resultant gel was charged into a stainless steel autoclave with a Teflon liner. The crystallization was then conducted at 175 °C for 12 days under static conditions. The solid product was filtered, washed with abundant water, and dried at 100 °C. The solids were calcined at 580 °C for 5 h in air.

Cu-exchange treatments

The Na-containing CHA calcined solids were first exchanged with a 2M aqueous solution of ammonium nitrate (NH₄Cl, Sigma-Aldrich, 99% by weight) with a liquid/solid ratio of 10, maintaining the mixture at 80 °C for 2 hours under agitation. Afterwards, the solids were recovered by filtration. 0.3 g of the Na-free zeolites was introduced in 30 ml of an aqueous solution of Cu(CH₃COO)₂·H₂O [14.1 mg of Cu(CH₃COO)₂·H₂O dissolved in 30 ml of water or 28.3 mg of Cu(CH₃COO)₂·H₂O dissolved in 30 ml of water for materials containing ~1.5 or 3%wt Cu, respectively], maintaining a solid/liquid ratio of 10 g/l at 80 °C for 24 h. Finally, the solids were filtered and washed with distilled water, dried and calcined at 550 °C in air for 4 h.

Characterization

Powder X-ray diffraction (PXRD) measurements were performed with a multi sample Philips X'Pert diffractometer equipped with a graphite monochromator, operating at 40 kV and 35 mA, and using Cu K α radiation ($\lambda = 0.1542$ nm). The PXRD patterns reveal the good crystallization of the CHA materials (see Figure S7 in the Supporting Information), all of them presenting particle sizes within the sub-micron scale (below 1 μm , see Figure S7 and Table S4 in the Supporting Information). Chemical analyses were carried out in a Varian 715-ES ICP-Optical Emission spectrometer, after solid dissolution in HNO₃/HCl/HF aqueous solution. Nitrogen adsorption isotherms at -196 °C were measured on a Micromeritics ASAP 2020 with a manometric adsorption analyser to determinate the textural properties of the samples. The morphology of the samples was studied by field emission scanning electron microscopy (FESEM) using a ZEISS Ultra-55 microscope.

Catalytic evaluation

The catalytic activity was evaluated for the selective catalytic reduction (SCR) of NO_x with NH₃ in a fixed bed, quartz tubular reactor with ~ 1 cm inner diameter. 20 mg sieve fractionated catalysts (200-400 μm) were placed between 0.6 of silicon carbide fractions (SiC, Fisher Chemical, 200-400 μm) generating an overall bed height of ~ 1.2 cm. The catalysts were introduced in the reactor and heated up to 550 °C in a 300 mL/min flow of nitrogen and maintained at this temperature for one hour. Afterwards, the feed was admitted over the catalyst with an overall flow of 600 mL/min. The feed composition for the catalytic tests performed over the Cu-containing catalysts was 500 ppm NO, 550 ppm NH₃, 7% O₂ and 5% H₂O, resulting in a very high space velocity (GHSV=1800000 ml/h.grcat). The evaluated reaction temperatures were 190, 180 and 170 °C. The conversion of NO was measured under steady state conversion at each temperature using a chemiluminescence detector (Thermo 62C). The TOF were estimated by dividing the moles of NO molecules converted per second by the moles of Cu atoms in the catalysts, according to

$$TOF = \frac{\text{moles NO converted/s}}{\text{moles Cu}} \quad (2)$$

From the low temperature NO conversion results, the rate constants (k) can be calculated using a first-order kinetic equation, as described previously in the literature:⁸⁸

$$k = -\frac{F_0}{[NO]_0 W} \ln(1 - X) \quad (3)$$

where F_0 is the molar NO feed rate, $[NO]_0$ is the molar concentration at the inlet, W is the catalyst amount (gr) and X is the NO conversion. The Arrhenius equation was employed to estimate the apparent activation energies (E_a) after its linearization as follows:

$$k = A e^{-E_a/RT} \quad (4)$$

$$\ln k = \ln A - \frac{E_a}{R} \left(\frac{1}{T} \right) \quad (5)$$

where A is the pre-exponential factor, R is the universal gas constant and T denotes the absolute temperature associated with the reaction (in Kelvin).

Data availability

The experimental and computational data that support the findings of this study are available from the corresponding author upon reasonable request. The datasets generated during this study are available at https://figshare.com/projects/Dataset_and_machine_learning_potential_Cu-CHA/167645. The code used for this study can be downloaded from <https://github.com/learningmatter-mit/NeuralForceField>.

References

- (1) Sushkevich, V. L.; Palagin, D.; Ranocchiari, M.; Van Bokhoven, J. A. Selective anaerobic oxidation of methane enables direct synthesis of methanol. *Science* **2017**, *356*, 523–527.
- (2) Dinh, K. T.; Sullivan, M. M.; Narsimhan, K.; Serna, P.; Meyer, R. J.; Dincă, M.; Román-Leshkov, Y. Continuous Partial Oxidation of Methane to Methanol Catalyzed by Diffusion-Paired Copper Dimers in Copper-Exchanged Zeolites. *Journal of the American Chemical Society* **2019**, *141*, 11641–11650.
- (3) Dinh, K. T.; Sullivan, M. M.; Serna, P.; Meyer, R. J.; Román-Leshkov, Y. Breaking the Selectivity-Conversion Limit of Partial Methane Oxidation with Tandem Heterogeneous Catalysts. *ACS Catalysis* **2021**, *11*, 9262–9270.
- (4) Del Campo, P.; Martínez, C.; Corma, A. Activation and conversion of alkanes in the confined space of zeolite-type materials. *Chemical Society Reviews* **2021**, *50*, 8511–8595.
- (5) Ohyama, J.; Tsuchimura, Y.; Hirayama, A.; Iwai, H.; Yoshida, H.; Machida, M.; Nishimura, S.; Kato, K.; Takahashi, K. Relationships among the Catalytic Performance, Redox Activity, and Structure of Cu-CHA Catalysts for the Direct Oxidation of Methane to Methanol Investigated Using In Situ XAFS and UV-Vis Spectroscopies. *ACS Catalysis* **2022**, *12*, 2454–2462.
- (6) Kwak, J. H.; Tonkyn, R. G.; Kim, D. H.; Szanyi, J.; Peden, C. H. F. Excellent activity and selectivity of Cu-SSZ-13 in the selective catalytic reduction of NO_x with NH₃. *Journal of Catalysis* **2010**, *275*, 187–190.
- (7) Paolucci, C.; Parekh, A. A.; Khurana, I.; Di Iorio, J. R.; Li, H.; Albarracín Caballero, J. D.; Shih, A. J.; Anggara, T.; Delgass, W. N.; Miller, J. T.; Ribeiro, F. H.; Gounder, R.; Schneider, W. F. Catalysis in a cage: Condition-dependent speciation and

- dynamics of exchanged Cu cations in SSZ-13 zeolites. *Journal of the American Chemical Society* **2016**, *138*, 6028–6048.
- (8) Gao, F.; Mei, D.; Wang, Y.; Szanyi, J.; Peden, C. H. Selective Catalytic Reduction over Cu/SSZ-13: Linking Homo- and Heterogeneous Catalysis. *Journal of the American Chemical Society* **2017**, *139*, 4935–4942.
- (9) Paolucci, C.; Khurana, I.; Parekh, A. A.; Li, S.; Shih, A. J.; Li, H.; Di Iorio, J. R.; Albarracin-Caballero, J. D.; Yezerets, A.; Miller, J. T.; Delgass, W. N.; Ribeiro, F. H.; Schneider, W. F.; Gounder, R. Dynamic multinuclear sites formed by mobilized copper ions in NO_x selective catalytic reduction. *Science* **2017**, *357*, 898–903.
- (10) Peden, C. H. Cu/Chabazite catalysts for ‘Lean-Burn’ vehicle emission control. *Journal of Catalysis* **2019**, *373*, 384–389.
- (11) Vennestrøm, P. N.; Thøgersen, J. R.; Gabrielsson, P. L.; Van Tendeloo, L.; Schütze, F.-W.; Moliner, M. Advances and perspectives from a decade of collaborative efforts on zeolites for selective catalytic reduction of NO_x. *Microporous and Mesoporous Materials* **2022**, 112336.
- (12) Moreno-González, M.; Millán, R.; Concepción, P.; Blasco, T.; Boronat, M. Spectroscopic Evidence and Density Functional Theory (DFT) Analysis of Low-Temperature Oxidation of Cu⁺ to Cu²⁺ NO_x in Cu-CHA Catalysts: Implications for the SCR-NO_x Reaction Mechanism. *ACS Catalysis* **2019**, *9*, 2725–2738.
- (13) Chen, L.; Janssens, T. V.; Vennestrøm, P. N.; Jansson, J.; Skoglundh, M.; Grönbeck, H. A Complete Multisite Reaction Mechanism for Low-Temperature NH₃-SCR over Cu-CHA. *ACS Catalysis* **2020**, *10*, 5646–5656.
- (14) Borfecchia, E.; Beato, P.; Svelle, S.; Olsbye, U.; Lamberti, C.; Bordiga, S. Cu-CHA – a model system for applied selective redox catalysis. *Chemical Society Reviews* **2018**, *47*, 8097–8133.

- (15) Signorile, M.; Borfecchia, E.; Bordiga, S.; Berlier, G. Influence of ion mobility on the redox and catalytic properties of Cu ions in zeolites. *Chemical Science* **2022**, *13*, 10238–10250.
- (16) Millan, R.; Cnudde, P.; Hoffman, A. E.; Lopes, C. W.; Concepción, P.; Van Speybroeck, V.; Boronat, M. Theoretical and Spectroscopic Evidence of the Dynamic Nature of Copper Active Sites in Cu-CHA Catalysts under Selective Catalytic Reduction (NH₃-SCR-NO_x) Conditions. *Journal of Physical Chemistry Letters* **2020**, *11*, 10060–10066.
- (17) Millan, R.; Cnudde, P.; Speybroeck, V. v.; Boronat, M. Mobility and Reactivity of Cu+ Species in Cu-CHA Catalysts under NH₃-SCR-NO_x Reaction Conditions: Insights from AIMD Simulations. *JACS Au* **2021**, *1*, 1778–1787.
- (18) Martini, A.; Negri, C.; Bugarin, L.; Deplano, G.; Abasabadi, R. K.; Lomachenko, K. A.; Janssens, T. V.; Bordiga, S.; Berlier, G.; Borfecchia, E. Assessing the Influence of Zeolite Composition on Oxygen-Bridged Diamino Dicopper(II) Complexes in Cu-CHA DeNO_xCatalysts by Machine Learning-Assisted X-ray Absorption Spectroscopy. *Journal of Physical Chemistry Letters* **2022**, *13*, 6164–6170.
- (19) Krishna, S. H.; Goswami, A.; Wang, Y.; Jones, C. B.; Dean, D. P.; Miller, J. T.; Schneider, W. F.; Gounder, R.; Davidson, C. D. Influence of framework Al density in chabazite zeolites on copper ion mobility and reactivity during NO_x selective catalytic reduction with NH₃. *Nature Catalysis* *2023 6:3* **2023**, *6*, 276–285.
- (20) Marberger, A.; Petrov, A. W.; Steiger, P.; Elsener, M.; Kröcher, O.; Nachttegaal, M.; Ferri, D. Time-resolved copper speciation during selective catalytic reduction of NO on Cu-SSZ-13. *Nature Catalysis* *2018 1:3* **2018**, *1*, 221–227.
- (21) Becher, J.; Sanchez, D. F.; Doronkin, D. E.; Zengel, D.; Meira, D. M.; Pascarelli, S.; Grunwaldt, J. D.; Sheppard, T. L. Chemical gradients in automotive Cu-SSZ-13 cata-

- lysts for NO_x removal revealed by operando X-ray spectrotomography. *Nature Catalysis* **2020** *4:1* **2020**, *4*, 46–53.
- (22) Wu, Y.; Zhao, W.; Ahn, S. H.; Wang, Y.; Walter, E. D.; Chen, Y.; Derewinski, M. A.; Washton, N. M.; Rappé, K. G.; Wang, Y.; Mei, D.; Hong, S. B.; Gao, F. Interplay between copper redox and transfer and support acidity and topology in low temperature NH₃-SCR. *Nature Communications* **2023**, *14*, 1–13.
- (23) Axelrod, S.; Schwalbe-Koda, D.; Mohapatra, S.; Damewood, J.; Greenman, K. P.; Gómez-Bombarelli, R. Learning Matter: Materials Design with Machine Learning and Atomistic Simulations. *Accounts of Materials Research* **2022**, *3*, 343–357.
- (24) Schmidt, J.; Marques, M. R. G.; Botti, S.; Marques, M. A. L. Recent advances and applications of machine learning in solid-state materials science. *npj Computational Materials* **2019**, *5*, 83.
- (25) Ma, S.; Liu, Z.-P. Machine Learning for Atomic Simulation and Activity Prediction in Heterogeneous Catalysis: Current Status and Future. *ACS Catalysis* **2020**, 13213–13226.
- (26) Goldsmith, B. R.; Esterhuizen, J.; Liu, J.-X. X. J.; Bartel, C. J.; Sutton, C. Machine learning for heterogeneous catalyst design and discovery. *AIChE Journal* **2018**, *64*, 2311–2323.
- (27) Schlexer Lamoureux, P.; Winther, K. T.; Garrido Torres, J. A.; Streibel, V.; Zhao, M.; Bajdich, M.; Abild-Pedersen, F.; Bligaard, T. Machine Learning for Computational Heterogeneous Catalysis. *ChemCatChem* **2019**, *11*, 3581–3601.
- (28) Gu, G. H.; Noh, J.; Kim, S.; Back, S.; Ulissi, Z.; Jung, Y. Practical Deep-Learning Representation for Fast Heterogeneous Catalyst Screening. *The Journal of Physical Chemistry Letters* **2020**, *11*, 3185–3191.

- (29) Behler, J. Neural network potential-energy surfaces in chemistry: a tool for large-scale simulations. *Physical Chemistry Chemical Physics* **2011**, *13*, 17930.
- (30) Behler, J. First Principles Neural Network Potentials for Reactive Simulations of Large Molecular and Condensed Systems. *Angewandte Chemie International Edition* **2017**, *56*, 12828–12840.
- (31) Botu, V.; Batra, R.; Chapman, J.; Ramprasad, R. Machine learning force fields: Construction, validation, and outlook. *Journal of Physical Chemistry C* **2017**, *121*, 511–522.
- (32) Mueller, T.; Hernandez, A.; Wang, C. Machine learning for interatomic potential models. *The Journal of Chemical Physics* **2020**, *152*, 50902.
- (33) von Lilienfeld, O. A.; Müller, K.-R. R.; Tkatchenko, A. Exploring chemical compound space with quantum-based machine learning. *Nature Reviews Chemistry* **2020**, *4*, 347–358.
- (34) Noé, F.; Olsson, S.; Köhler, J.; Wu, H. Boltzmann generators: Sampling equilibrium states of many-body systems with deep learning. *Science* **2019**, *365*, eaaw1147.
- (35) Jensen, K. F.; Coley, C. W.; Eyke, N. S. Autonomous discovery in the chemical sciences part I: Progress. *Angewandte Chemie International Edition* **2019**, *59*, 2858–22893.
- (36) Butler, K. T.; Davies, D. W.; Cartwright, H.; Isayev, O.; Walsh, A. Machine learning for molecular and materials science. *Nature* **2018**, *559*, 547–555.
- (37) Erlebach, A.; Nachtigall, P.; Grajciar, L. Accurate large-scale simulations of siliceous zeolites by neural network potentials. *npj Computational Materials* **2022**, *8*, 1–12.
- (38) Moliner, M.; Román-Leshkov, Y.; Corma, A. Machine Learning Applied to Zeolite

- Synthesis: The Missing Link for Realizing High-Throughput Discovery. *Accounts of Chemical Research* **2019**, *52*, 2971–2980.
- (39) Chmiela, S.; Sauceda, H. E.; Müller, K.-R.; Tkatchenko, A. Towards exact molecular dynamics simulations with machine-learned force fields. *Nature Communications* **2018**, *9*, 3887.
- (40) Sosso, G. C.; Miceli, G.; Caravati, S.; Behler, J.; Bernasconi, M. Neural network interatomic potential for the phase change material GeTe. *Physical Review B* **2012**, *85*, 174103.
- (41) Bernstein, N.; Bhattarai, B.; Csányi, G.; Drabold, D. A.; Elliott, S. R.; Deringer, V. L.; Bernstein, N.; Bhattarai, B.; Drabold, R. D. A.; Csányi, G.; Deringer, V. L.; Elliott, S. R. Quantifying Chemical Structure and Machine-Learned Atomic Energies in Amorphous and Liquid Silicon. *Angewandte Chemie International Edition* **2019**, *58*, 7057–7061.
- (42) Smith, J. S.; Isayev, O.; Roitberg, A. E. ANI-1, A data set of 20 million calculated off-equilibrium conformations for organic molecules. *Scientific Data* **2017**, *4*, 170193.
- (43) Smith, J. S.; Isayev, O.; Roitberg, A. E. ANI-1: an extensible neural network potential with DFT accuracy at force field computational cost. *Chemical Science* **2017**, *8*, 3192–3203.
- (44) Smith, J. S.; Nebgen, B. T.; Zubatyuk, R.; Lubbers, N.; Devereux, C.; Barros, K.; Tretiak, S.; Isayev, O.; Roitberg, A. E. Approaching coupled cluster accuracy with a general-purpose neural network potential through transfer learning. *Nature Communications* **2019**, *10*, 1–8.
- (45) Devereux, C.; Smith, J. S.; Huddleston, K. K.; Barros, K.; Zubatyuk, R.; Isayev, O.; Roitberg, A. E. Extending the Applicability of the ANI Deep Learning Molecular Po-

- tential to Sulfur and Halogens. *Journal of Chemical Theory and Computation* **2020**, *16*, 4192–4202.
- (46) Schütt, K. T.; Arbabzadah, F.; Chmiela, S.; Müller, K. R.; Tkatchenko, A. Quantum-chemical insights from deep tensor neural networks. *Nature Communications* **2017**, *8*, 6–13.
- (47) Schütt, K. T.; Kessel, P.; Gastegger, M.; Nicoli, K. A.; Tkatchenko, A.; Müller, K. R. SchNetPack: A Deep Learning Toolbox for Atomistic Systems. *Journal of Chemical Theory and Computation* **2019**, *15*, 448–455.
- (48) Zhang, L.; Han, J.; Wang, H.; Car, R.; Weinan, E. Deep Potential Molecular Dynamics: A Scalable Model with the Accuracy of Quantum Mechanics. *Physical Review Letters* **2018**, *120*, 143001.
- (49) Chen, C.; Ye, W.; Zuo, Y.; Zheng, C.; Ong, S. P. Graph Networks as a Universal Machine Learning Framework for Molecules and Crystals. *Chemistry of Materials* **2019**, *31*, 3564–3572.
- (50) Klicpera, J.; Groß, J.; Günnemann, S. Directional message passing for molecular graphs. ICLR. 2020; pp 1–13.
- (51) Qiao, Z.; Welborn, M.; Anandkumar, A.; Manby, F. R.; Miller, T. F. OrbNet: Deep learning for quantum chemistry using symmetry-adapted atomic-orbital features. *The Journal of Chemical Physics* **2020**, *153*, 124111.
- (52) Schütt, K. T.; Unke, O. T.; Gastegger, M. Equivariant message passing for the prediction of tensorial properties and molecular spectra. *arXiv preprint arXiv:2102.03150* **2021**,
- (53) Batzner, S.; Musaelian, A.; Sun, L.; Geiger, M.; Mailoa, J. P.; Kornbluth, M.; Moli-

- nari, N.; Smidt, T. E.; Kozinsky, B. E(3)-Equivariant Graph Neural Networks for Data-Efficient and Accurate Interatomic Potentials. *Nature Communications* **2021**, *13*, 1–11.
- (54) Artrith, N.; Urban, A. An implementation of artificial neural-network potentials for atomistic materials simulations: Performance for TiO₂. *Computational Materials Science* **2016**, *114*, 135–150.
- (55) Vandenhaute, S.; Cools-Ceuppens, M.; DeKeyser, S.; Verstraelen, T.; Van Speybroeck, V. Machine learning potentials for metal-organic frameworks using an incremental learning approach. *npj Computational Materials* **2023**, *9*, 1–8.
- (56) Bocus, M.; Goeminne, R.; Lataire, A.; Cools-Ceuppens, M.; Verstraelen, T.; Van Speybroeck, V. Nuclear quantum effects on zeolite proton hopping kinetics explored with machine learning potentials and path integral molecular dynamics. *Nature Communications* **2023**, *14*, 1–11.
- (57) Winter, G.; Gómez-Bombarelli, R. Simulations with machine learning potentials identify the ion conduction mechanism mediating non-Arrhenius behavior in LGPS. 2022; preprint, <http://arxiv.org/abs/2211.05713v2>.
- (58) Gastegger, M.; Marquetand, P. High-Dimensional Neural Network Potentials for Organic Reactions and an Improved Training Algorithm. *Journal of Chemical Theory and Computation* **2015**, *11*, 2187–2198.
- (59) Ang, S. J.; Wang, W.; Schwalbe-Koda, D.; Axelrod, S.; Gómez-Bombarelli, R. Active learning accelerates ab initio molecular dynamics on reactive energy surfaces. *Chem* **2021**, *7*, 1–32.
- (60) Du, X.; Damewood, J. K.; Lunger, J. R.; Millan, R.; Yildiz, B.; Li, L.; Gómez-Bombarelli, R. Machine-learning-accelerated simulations enable heuristic-free surface reconstruction. 2023; preprint, <https://arxiv.org/abs/2305.07251>.

- (61) Behler, J. Constructing high-dimensional neural network potentials: A tutorial review. *International Journal of Quantum Chemistry* **2015**, *115*, 1032–1050.
- (62) Smith, J. S.; Nebgen, B.; Lubbers, N.; Isayev, O.; Roitberg, A. E. Less is more: Sampling chemical space with active learning. *Journal of Chemical Physics* **2018**, *148*, 241733.
- (63) Schran, C.; Brezina, K.; Marsalek, O. Committee neural network potentials control generalization errors and enable active learning. *Journal of Chemical Physics* **2020**, *153*, 104105.
- (64) Musil, F.; Willatt, M. J.; Langovoy, M. A.; Ceriotti, M. Fast and Accurate Uncertainty Estimation in Chemical Machine Learning. *Journal of Chemical Theory and Computation* **2019**, *15*, 906–915.
- (65) Peterson, A. A.; Christensen, R.; Khorshidi, A. Addressing uncertainty in atomistic machine learning. *Physical Chemistry Chemical Physics* **2017**, *19*, 10978–10985.
- (66) Lookman, T.; Balachandran, P. V.; Xue, D.; Yuan, R. Active learning in materials science with emphasis on adaptive sampling using uncertainties for targeted design. *npj Computational Materials* **2019**, *5*, 21.
- (67) Shapeev, A.; Gubaev, K.; Tsymbalov, E.; Podryabinkin, E. In *Machine Learning Meets Quantum Physics*; Schütt, K. T., Chmiela, S., von Lilienfeld, O. A., Tkatchenko, A., Tsuda, K., Müller, K.-R., Eds.; Springer International Publishing: Cham, 2020; pp 309–329.
- (68) Imbalzano, G.; Zhuang, Y.; Kapil, V.; Rossi, K.; Engel, E. A.; Grasselli, F.; Ceriotti, M. Uncertainty estimation for molecular dynamics and sampling. *The Journal of Chemical Physics* **2021**, *154*, 74102.

- (69) Wang, W.; Yang, T.; Harris, W. H.; Gómez-Bombarelli, R. Active learning and neural network potentials accelerate molecular screening of ether-based solvate ionic liquids. *Chemical Communications* **2020**, *56*, 8920–8923.
- (70) Wang, W.; Axelrod, S.; Gómez-Bombarelli, R. Differentiable Molecular Simulations for Control and Learning. 2020; preprint, <http://arxiv.org/abs/2003.00868>.
- (71) Schwalbe-Koda, D.; Tan, A. R.; Gómez-Bombarelli, R. Differentiable sampling of molecular geometries with uncertainty-based adversarial attacks. *Nature Communications* **2021**, *12*, 1–12.
- (72) Tan, A. R.; Urata, S.; Goldman, S.; Dietschreit, J. C. B.; Gómez-Bombarelli, R. Single-model uncertainty quantification in neural network potentials does not consistently outperform model ensembles. 2023; preprint, <https://arxiv.org/abs/2305.01754v1>.
- (73) McInnes, L.; Healy, J.; Saul, N.; Großberger, L. UMAP: Uniform Manifold Approximation and Projection. *Journal of Open Source Software* **2018**, *3*, 861.
- (74) Xie, T.; Grossman, J. C. Crystal Graph Convolutional Neural Networks for an Accurate and Interpretable Prediction of Material Properties. *Physical Review Letters* **2018**, *120*, 145301.
- (75) Fu, X.; Wu, Z.; Wang, W.; Xie, T.; Keten, S.; Gomez-Bombarelli, R.; Jaakkola, T. Forces are not Enough: Benchmark and Critical Evaluation for Machine Learning Force Fields with Molecular Simulations. 2022; preprint, <https://arxiv.org/abs/2210.07237v1>.
- (76) Shwan, S.; Skoglundh, M.; Lundegaard, L. F.; Tiruvalam, R. R.; Janssens, T. V.; Carlsson, A.; Vennestrøm, P. N. Solid-State Ion-Exchange of Copper into Zeolites Facilitated by Ammonia at Low Temperature. *ACS Catalysis* **2015**, *5*, 16–19.

- (77) Vennestrøm, P. N.; Lundegaard, L. F.; Tyrsted, C.; Bokarev, D. A.; Mytareva, A. I.; Baeva, G. N.; Stakheev, A. Y.; Janssens, T. V. The Role of Protons and Formation of $\text{Cu}(\text{NH}_3)_2^+$ During Ammonia-Assisted Solid-State Ion Exchange of Copper(I) Oxide into Zeolites. *Topics in Catalysis* **2019**, *62*, 100–107.
- (78) Šípka, M.; Dietschreit, J. C. B.; Grajciar, L.; Gómez-Bombarelli, R. Differentiable Simulations for Enhanced Sampling of Rare Events. **2023**,
- (79) Zhang, Y.; Yang, W. Comment on “Generalized Gradient Approximation Made Simple”. *Physical Review Letters* **1998**, *80*, 890.
- (80) Grimme, S.; Antony, J.; Ehrlich, S.; Krieg, H. A consistent and accurate ab initio parametrization of density functional dispersion correction (DFT-D) for the 94 elements H-Pu. *The Journal of Chemical Physics* **2010**, *132*, 154104.
- (81) Vandevondele, J.; Krack, M.; Mohamed, F.; Parrinello, M.; Chassaing, T.; Hutter, J. Quickstep: Fast and accurate density functional calculations using a mixed Gaussian and plane waves approach. *Computer Physics Communications* **2005**, *167*, 103–128.
- (82) Lippert, G.; Hutter, J.; Parrinello, M. The Gaussian and augmented-plane-wave density functional method for ab initio molecular dynamics simulations. *Theoretical Chemistry Accounts* **1999**, *103*, 124–140.
- (83) Goedecker, S.; Teter, M. Separable dual-space Gaussian pseudopotentials. *Physical Review B* **1996**, *54*, 1703.
- (84) Martyna, G. J.; Klein, M. L.; Tuckerman, M. Nosé-Hoover chains: The canonical ensemble via continuous dynamics. *The Journal of Chemical Physics* **1992**, *97*, 2635–2643.
- (85) Hoover, W. G.; Ladd, A. J. C.; Moran, B. High-Strain-Rate Plastic Flow Studied via Nonequilibrium Molecular Dynamics. *Physical Review Letters* **1982**, *48*, 1818–1820.

- (86) Torrie, G. M.; Valleau, J. P. Nonphysical sampling distributions in Monte Carlo free-energy estimation: Umbrella sampling. *Journal of Computational Physics* **1977**, *23*, 187–199.
- (87) Kumar, S.; Rosenberg, J. M.; Bouzida, D.; Swendsen, R. H.; Kollman, P. A. THE weighted histogram analysis method for free energy calculations on biomolecules. I. The method. *Journal of Computational Chemistry* **1992**, *13*, 1011–1021.
- (88) Long, R. Q.; Yang, R. T. Selective Catalytic Reduction of NO with Ammonia over Fe³⁺-Exchanged Mordenite (Fe-MOR): Catalytic Performance, Characterization, and Mechanistic Study. *Journal of Catalysis* **2002**, *207*, 274–285.

Acknowledgement

R.M acknowledges the Margarita Salas grant from the Ministerio de Universidades, Spain, funded by the European Union-Next Generation EU. The authors are grateful for computation time allocated on the MIT SuperCloud cluster, the MIT Engaging cluster at the Massachusetts Green High Performance Computing Center (MGHPCC); and Summit at the Oakridge Leadership Computing Facility through the 2021 ALCC DOE program. R.G-B. thanks the Jeffrey Cheah Career Development Chair. R.M thanks Gavin Winter for assistance during the training of NNP and processing of the MD simulations, and Simon Axelrod for implementing PaiNN. M.B. and M.M. thank financial support from Spanish Government through CEX2021-001230-S, PID2020-112590GB-C21, PID2021-122755OB-I00 and TED2021-130739B-I00 (MCIN/AEI/FEDER, UE), and from CSIC through the I-link+ Program (LINKA20381). E.B. acknowledges the Spanish Government-MCIU for a FPI scholarship (PRE2019-088360). The Electron Microscopy Service of the UPV is acknowledged for its help in sample characterization.

Author Contributions

R.G-B. and M. B. designed the project. R. M. developed the NNP and performed all simulations, supervised by R.G.-B. M. M. directed the zeolite synthesis and catalytic experiments. E. B. performed the zeolite synthesis and catalytic experiments. R.M. wrote the first manuscript draft with contributions from R.G.-B. and M.B. All authors participated in the discussion and interpretation of the results, and contributed to the manuscript preparation and revision.

Competing interests

The authors declare no competing interests.

Supporting Information Available

Table S1: Chemical composition, cationic species and molecules included in the triclinic $T_{96}O_{192}$ supercell models used for active learning and adversarial attack.

Formulas	Si/Al	Al	Si	$[\text{Cu}(\text{NH}_3)_2]^+$	NH_4^+	NH_3	H^+
$\text{H}_2\text{Al}_2\text{O}_{192}\text{Si}_{94}$	47	2	94	0	0	0	2
$\text{H}_8\text{Al}_2\text{N}_2\text{O}_{192}\text{Si}_{94}$	47	2	94	0	2	0	0
$\text{H}_{12}\text{Al}_3\text{N}_3\text{O}_{192}\text{Si}_{93}$	31	3	93	0	3	0	0
$\text{H}_{15}\text{Al}_3\text{N}_4\text{O}_{192}\text{Si}_{93}$	31	3	93	0	3	1	0
$\text{H}_{18}\text{Al}_3\text{N}_5\text{O}_{192}\text{Si}_{93}$	31	3	93	0	3	2	0
$\text{H}_{28}\text{Al}_7\text{N}_7\text{O}_{192}\text{Si}_{89}$	12.7	7	89	0	7	0	0
$\text{H}_{12}\text{Al}_2\text{Cu}_2\text{N}_4\text{O}_{192}\text{Si}_{94}$	47	2	94	2	0	0	0
$\text{H}_{10}\text{Al}_2\text{Cu}_1\text{N}_3\text{O}_{192}\text{Si}_{94}$	47	2	94	1	1	0	0
$\text{H}_{18}\text{Al}_2\text{Cu}_2\text{N}_6\text{O}_{192}\text{Si}_{94}$	47	2	94	2	0	2	0
$\text{H}_{18}\text{Al}_3\text{Cu}_2\text{N}_6\text{O}_{192}\text{Si}_{93}$	31	3	93	2	1	0	0

Table S2: Free energies of activation (ΔG_{act}) and reaction (ΔG) for the diffusion of a $[\text{Cu}(\text{NH}_3)_2]^+$ complex between two neighboring cages through 8R windows with different Al distribution obtained from NNP-based biased simulations at 423 K.

Al distribution	ΔG_{act} (kcal/mol)	ΔG (kcal/mol)
SR1	3.9	0.4
SR2	4.6	1.7
SR3	5.4	2.3
SR4	4.1	0.5
DR1	6.1	3.2
DR2	6.7	2.9
DR3	6.4	3.2
DR4	5.4	-0.7
S4R	7.3	4.5
S6R	6.4	5.4

Table S3: Chemical composition, cationic species and molecules included in the triclinic $T_{768}O_{1536}$ supercell models used for NNP-based regular molecular dynamics simulations.

Name	Formulas	Si/Al	Al	Si	$[\text{Cu}(\text{NH}_3)_2]^+$	NH_4^+	NH_3	H^+
L20	$\text{H}_{144}\text{Al}_{26}\text{Cu}_{20}\text{N}_{46}\text{O}_{1536}\text{Si}_{742}$	28.5	26	742	20	6	0	0
L4	$\text{H}_{112}\text{Al}_{26}\text{Cu}_4\text{N}_{30}\text{O}_{1536}\text{Si}_{742}$	28.5	26	742	4	22	0	0
M20	$\text{H}_{240}\text{Al}_{50}\text{Cu}_{20}\text{N}_{70}\text{O}_{1536}\text{Si}_{718}$	14.3	50	718	20	30	0	0
M4	$\text{H}_{208}\text{Al}_{50}\text{Cu}_4\text{N}_{54}\text{O}_{1536}\text{Si}_{718}$	14.3	50	718	4	46	0	0
M20-H+	$\text{H}_{150}\text{Al}_{50}\text{Cu}_{20}\text{N}_{40}\text{O}_{1536}\text{Si}_{718}$	14.3	50	718	20	0	0	30
M20-NH3	$\text{H}_{423}\text{Al}_{50}\text{Cu}_{20}\text{N}_{131}\text{O}_{1536}\text{Si}_{718}$	14.3	50	718	20	30	60	0
H6R	$\text{H}_{312}\text{Al}_{68}\text{Cu}_{20}\text{N}_{88}\text{O}_{1536}\text{Si}_{700}$	10.3	68	700	20	48	0	0
H8R	$\text{H}_{312}\text{Al}_{68}\text{Cu}_{20}\text{N}_{88}\text{O}_{1536}\text{Si}_{700}$	10.3	68	700	20	48	0	0
HR	$\text{H}_{312}\text{Al}_{68}\text{Cu}_{20}\text{N}_{88}\text{O}_{1536}\text{Si}_{700}$	10.3	68	700	20	48	0	0
HB	$\text{H}_{312}\text{Al}_{68}\text{Cu}_{20}\text{N}_{88}\text{O}_{1536}\text{Si}_{700}$	10.3	68	700	20	48	0	0

Table S4: Chemical composition and physico-chemical properties of the synthesized CHA zeolites.

Sample	Si/Al	Al/ <i>cha</i> cage	Crystal size (nm)	BET surface area (m^2/g)	Micropore area (m^2/g)	Micropore volume (cm^3/g)
CHA07	7.3	1.4	~100	562	532	0.26
CHA13	12.7	0.9	~400-800	556	551	0.27
CHA23	23.3	0.5	~100	550	490	0.25

Table S5: Chemical composition of the Cu-exchanged CHA zeolites.

Sample	Si/Al	%wt Cu	Cu/Al	Al/ <i>cha</i> cage
CHA07_1.5Cu	7.3	1.58	0.11	0.16
CHA07_3.0Cu	7.3	2.92	0.20	0.30
CHA13_1.5Cu	12.7	1.55	0.18	0.17
CHA23_1.5Cu	23.3	1.54	0.35	0.17

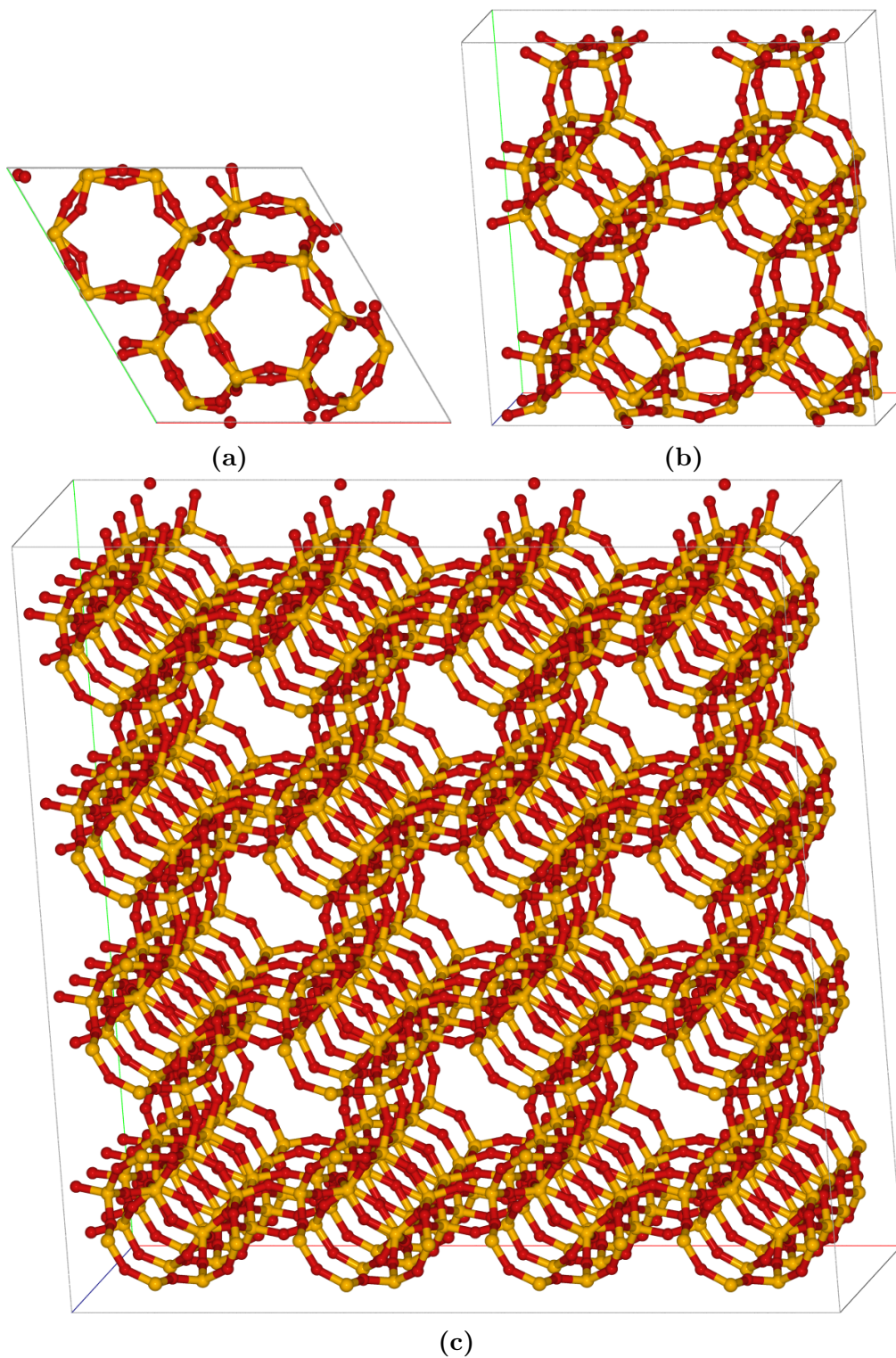


Figure S1: Representation of the three types of base lattices used for umbrella sampling simulations (a and b) and for unbiased MD simulations (c). The representations correspond to the all-silica CHA, however, the models used in this work include different combinations of Al number and locations starting from this base lattices, as explained in the main text. Color code: Si and O are depicted as orange and red respectively.

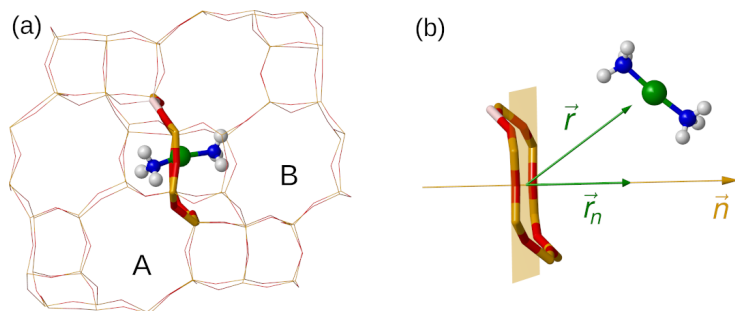


Figure S2: Diffusion of $[\text{Cu}(\text{NH}_3)_2]^+$ complex from cage A ($\xi < 0$) to cage B ($\xi > 0$). (b) Representation of the collective variable ξ describing the $[\text{Cu}(\text{NH}_3)_2]^+$ diffusion through the 8R window (transparent yellow plane)

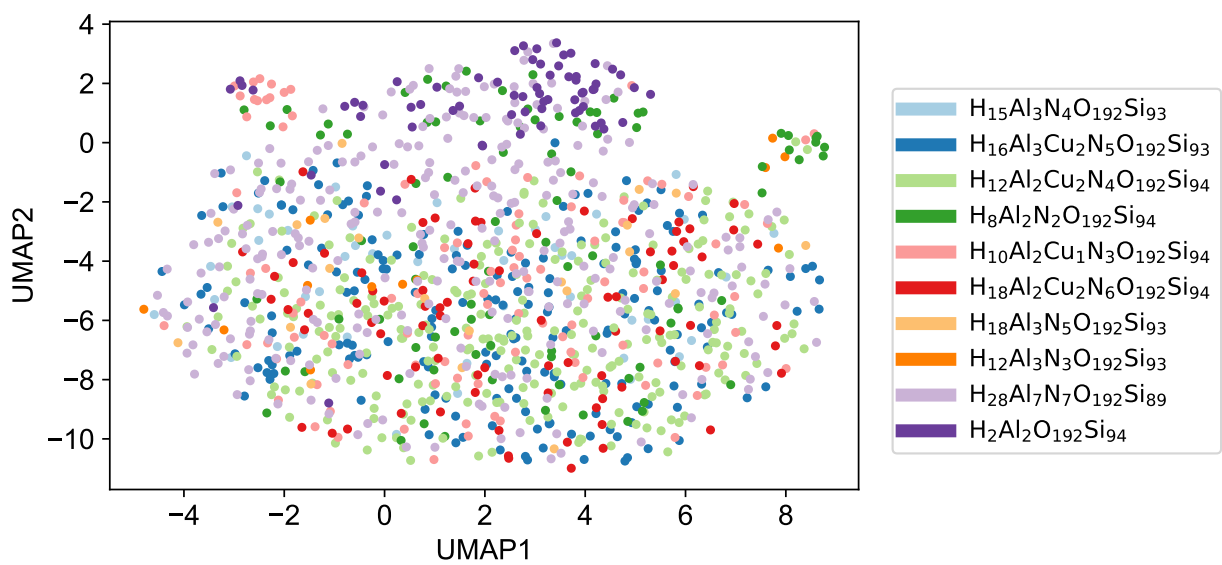


Figure S3: UMAP plot for the feature vectors of Al atoms from $\sim 1\%$ of the dataset. Both axes are on the same scale.

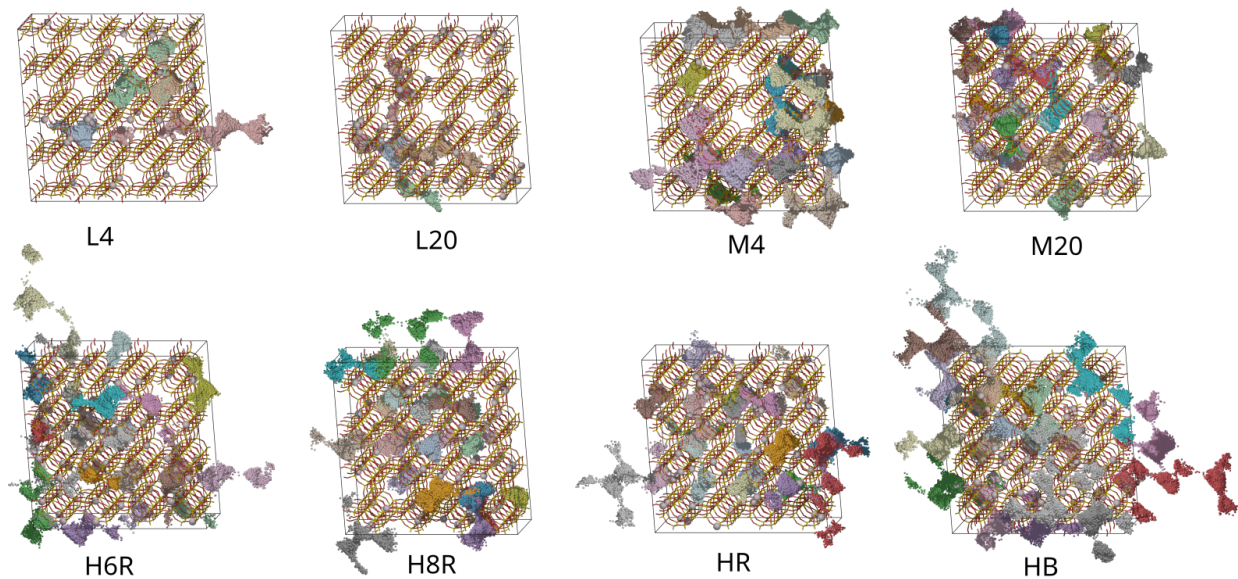


Figure S4: Scatter plots showing the regions visited by Cu^+ in the simulations run at 500 K for 5 ns. Color code: Si, O, and Al atoms are depicted as orange, red and light brown. Each Cu^+ cation is represented with a random color.

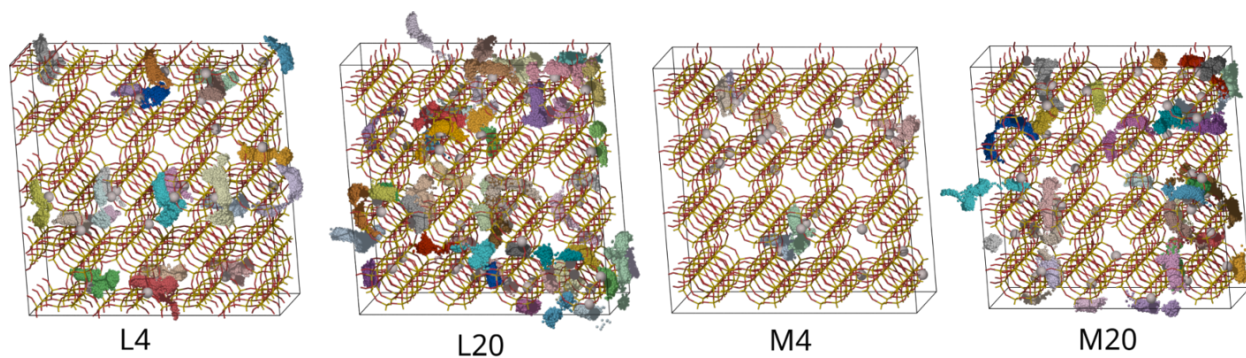


Figure S5: Scatter plots showing the regions visited by NH_4^+ in the simulations run at 500 K for 5 ns. Color code: Si, O, and Al atoms are depicted as orange, red and light brown. Each NH_4^+ is represented with a random color.

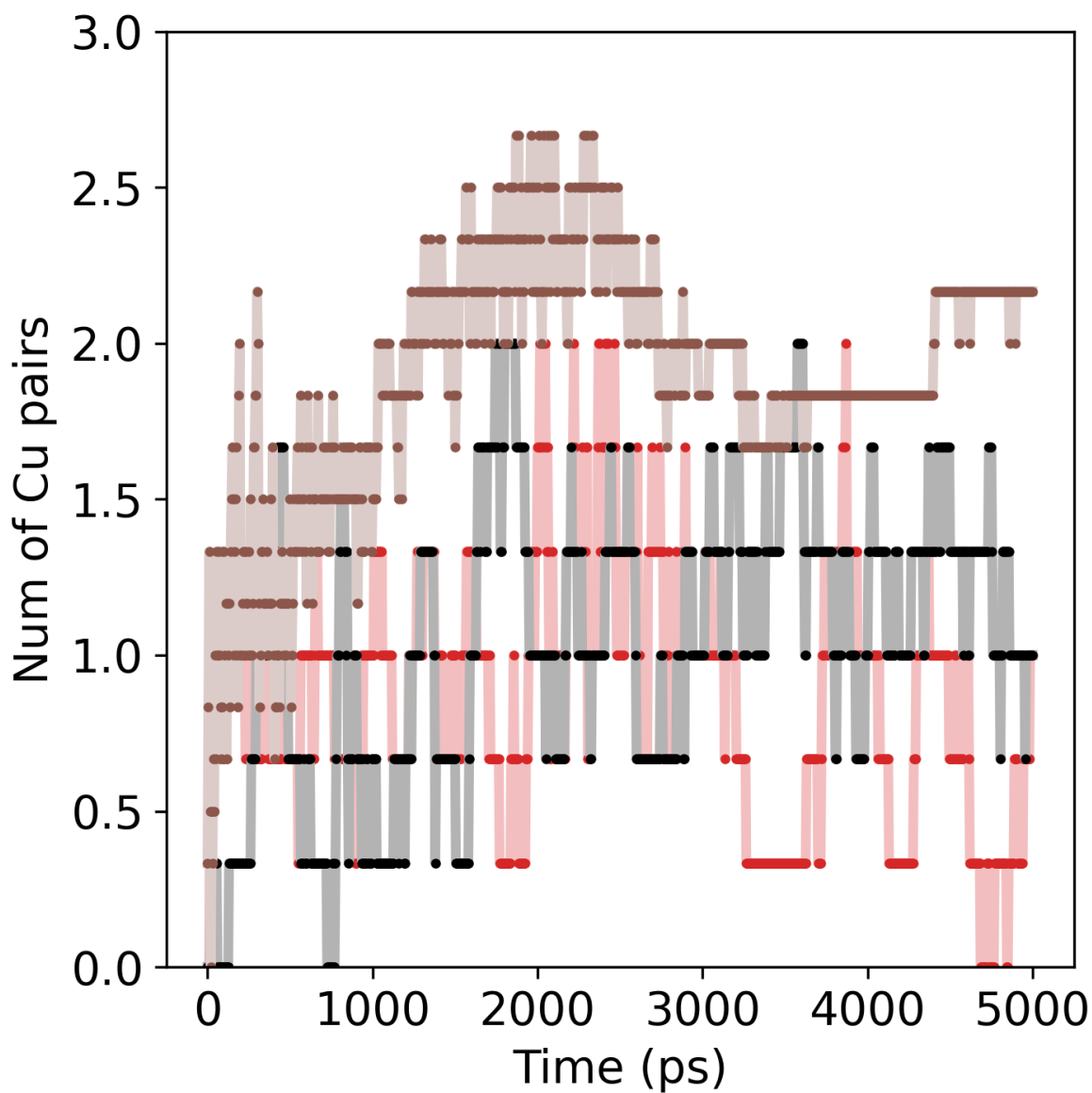


Figure S6: Time evolution of the average number of $[\text{Cu}(\text{NH}_3)_2]^+$ pairs in the same cage for the models M20 (red), M20-H+ (black), M20-NH3 (brown), in unbiased MD simulations at 500 K.

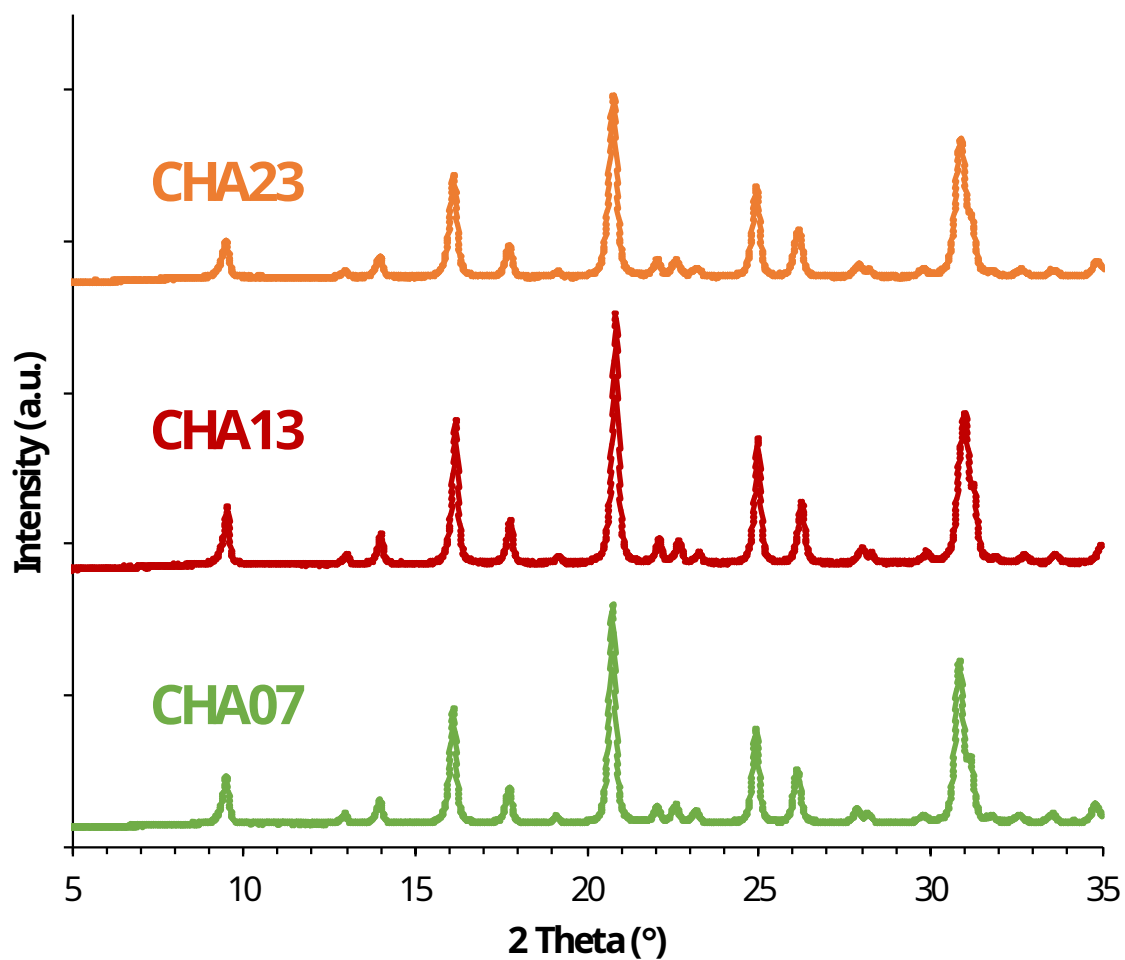


Figure S7: PXR D patterns of the synthesized CHA zeolites

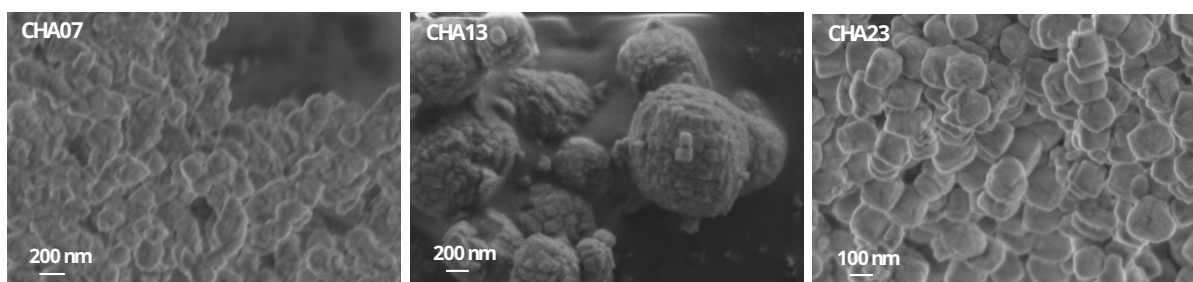
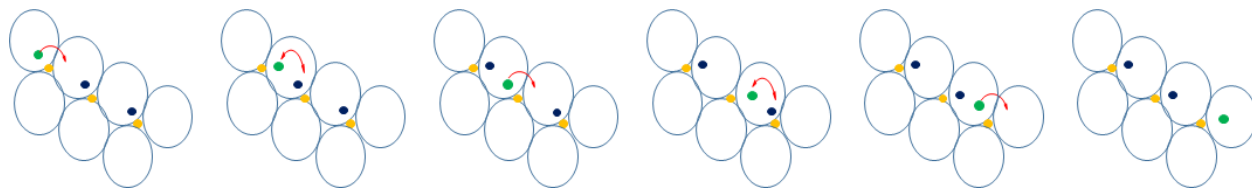


Figure S8: FESEM images of the synthesized CHA zeolites



Scheme S1: Representation of long-range $[\text{Cu}(\text{NH}_3)_2]^+$ migration assisted by NH_4^+ . Al, Cu^+ and NH_4^+ are represented with yellow, green and blue balls, respectively.